

HYDRODYNAMICS OVER A PATCH STRUCTURE ON AN INTERTIDAL MUSSEL BED

PHYSICAL GEOGRAPHY – MSc THESIS

FEBRUARY 6, 2013

Author:
EDWIN DROST (3564479)

Supervisors:
MAARTEN VAN DER VEGT
JASPER DONKER



Universiteit Utrecht

Abstract

The Mosselwad project investigates the stability and restoration opportunities of mussel beds in the Dutch Wadden Sea. The experiments in this study, which were performed in the framework of this project, investigate the key hydrodynamic processes for the survival chances of mussel beds and especially the possible important effects of the mussel bed patch size on hydrodynamical forcing. Previous studies on hydrodynamic processes in relation to mussel beds were performed in flume experiments. This limits the possibilities of expanding these results to field conditions. Therefore a field study was performed on a young intertidal mussel bed near Texel in the Dutch Wadden Sea to obtain key hydrodynamic parameters. The length and width of the investigated mussel patch was $\sim 20m$, while the elevation of the patch above its surroundings was $\sim 10cm$. Turbulent kinetic energy dissipation rates were estimated from obtained measurements and used to calculate turbulence parameters and bed roughness values. Results showed higher current velocities above the patch than downstream of the patch and further away of the patch. Also higher turbulent kinetic energy values and a higher eddy viscosity on the patch than downstream of the patch were observed. Obtained wave heights on the site were small and effects of the mussel patch on the wave height were not observed, however even orbital velocities of these small waves dominated the total bed shear stress and generated additional turbulent kinetic energy. On the other hand observed current velocities showed weak indications for flow routing, however the measurement setup was insufficient to formulate strong conclusions. The higher turbulent kinetic energy values and eddy viscosity above the mussel patch shows that vertical turbulent mixing was enhanced as flow passed the upstream patch boundary, while flow still experienced a high roughness length behind the downstream patch boundary due to flow recovery effects. Overall, the results of this study confirm the importance of patch boundaries for the turbulent mixing and thus food supply of the mussels. Additionally flow routing might play a major role for patch structures, but additional research is required to support this assumption.

Contents

1	Introduction	3
1.1	Mussel bed behavior and environmental factors	4
1.2	Hydrodynamic and morphological processes	5
1.3	Research questions	6
2	Theory	8
2.1	Turbulent flow properties	8
2.2	Current boundary layer	9
2.3	Interaction between currents, waves and wind stress	10
2.4	Effects of an individual mussel and a covered mussel bed	14
2.5	Rough to smooth surface transition	15
2.6	Effects of flow routing	16
3	Materials and Methods	18
3.1	Field location	18
3.2	Equipment	19
3.3	Data processing	22
3.4	Bed level	24
3.5	Environmental conditions	24
3.6	Data selection	24
4	Results	27
4.1	Bathymetry	27
4.2	Tidal characteristics	27
4.3	Current velocities	30
4.3.1	Tide-dominated current with low wind exposure	34
4.3.2	Average tide with high wind exposure from a southwestern direction	34
4.3.3	Weak tide with high wind exposure from a southeastern direction	37
4.3.4	Vorticity	37
4.4	Waves	40
4.5	Turbulence	41
4.5.1	Dissipation of TKE and roughness	45
4.5.2	Reynolds stress and turbulent kinetic energy	48
4.5.3	Bed shear stress	51
5	Discussion	53
5.1	Effects of a mussel patch on hydrodynamics	53
5.2	Effects of a mussel patch on turbulent mixing	54
5.3	Implications of patchiness for mussel beds	57
5.4	Removing wave bias with pressure sensors	57
6	Conclusions	58
7	Recommendations	59
8	Acknowledgments	59

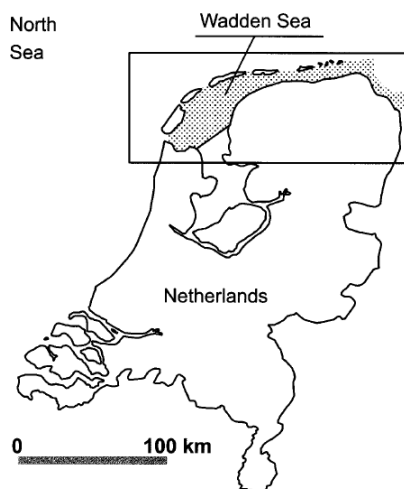


Figure 1: Location of the Wadden Sea in The Netherlands.

1 Introduction

The Mosselwad project is a co-operation between the Coastal & Marine Union - Netherlands, IMARES (Institute for Marine Resources and Ecosystem Studies), NIOZ (Netherlands Institute for Sea Research), SOVON (Dutch Centre for Field Ornithology) and the faculty of Geosciences of the University of Utrecht. The project focuses on determining factors to the survival chances of mussel beds and patches within a mussel bed in the Wadden Sea and eventually new mussel beds will be constructed and monitored. The survival chances of mussel beds are studied from an ecological and physical perspective and are related to nutrient availability, natural predators and hydrodynamic forcing. This research project describes key hydrodynamic processes that are determinative to the survival chances of mussel beds and particularly focuses on the possible important effects of mussel bed patches on hydrodynamical forcing.

The Dutch Wadden Sea is located in the northern part of The Netherlands (figure 1) and covers an area of about 2500 km^2 and of which 50 % can be characterized as intertidal sand and mud flats. The other parts are characterized by subtidal regions, inlets and channels, while the mainland is bordered by dikes. The tidal inlets between the barrier islands supply water from the North Sea into the Wadden Sea and drain water out of the Wadden Sea. The combination of these tidal channels and intertidal flats and a high availability of specific food sources for birds (benthic shellfish, worms and crustacea) makes the Wadden Sea one of the most important areas for several bird species [Brinkman et al., 2002]. An important benthic shellfish food sources for birds is the mussel. Mussels appear in intertidal mussel beds which are emerged during low water as well as in subtidal mussel beds. This paper focuses on intertidal mussel beds (example is shown in figure 2).



Figure 2: Example of a patchy intertidal mussel bed in the Dutch Wadden Sea.

1.1 Mussel bed behavior and environmental factors

Mussels are known as bio-engineers that are able to modify their immediate physical environment by altering currents, wave action and sediment transport. Other examples of bio-stabilizers are oyster reefs, macroalgal mats, microphytobenthos, salt marsh macrophytes and seagrass beds [Widdows and Brinsley, 2002]. The mussel in the Wadden Sea is the blue mussel (*Mytilus edulis*). Blue mussels reproduce themselves by producing more than a million eggs per individual animal, of which only a few will survive [Brinkman et al., 2002]. When the eggs are released in the water column they will develop into larvae that will be distributed by wind-driven and tidal currents [De Vooy, 1999]. The larvae will search a substratum to attach to when they are large enough (about 0.2 mm). The chances of finding a suitable substratum depend on the total amount of substratum that is available in the area, but not all suitable substratum will be used. Suitable substrata in the Wadden Sea consist of adult mussels or other benthic shellfish, which are favored but not always available, and even bare sand or silt [Pulfrich, 1995]. The hydrodynamic forces should not be too strong for the mussel larvae to settle successfully. After settlement the action radius of the mussels is reduced to only a few decimeters and the shells start to produce very strong byssus threads, which are used by the mussel to keep attached to each other and to the substratum.

Mussels feed themselves by filtering suspended particles from the water column, where the nutrients are attached to the suspended sediment particles and algae [Oost, 1995]. Most of these nutrients, that are dominantly produced by phytoplankton in the estuary area, arrive at mussel beds by tidal currents [Nienhuis, 1993]. Consequently the filtering of water by the mussels happens at a high rate of 100 liter per hour by 1 kg of mussels [Oost, 1995], whereupon the filtered sediments are excreted. These excreted sediments result in faces and pseudo-faces that contain larger grain sizes than before the filtering process. Because of the increased grain size the sediments will have a higher settling probability.

Most mussels are emerged for more than 50 % of the time. Brinkman et al. [2002] studied the habitat suitability in the Dutch Wadden Sea and found that higher elevated tidal flats have almost no mussel beds, although areas with low emersion times are less favorable for mussel bed as well. Several important parameters should be considered:

- Mussels can only feed themselves when they are submerged, so a large emersion time is disadvantageous for the supply of nutrients and therefore growth rates of the mussels.
- During emersion mussel beds are also more vulnerable for biological factors such as predation by birds [Hilgerloh et al., 1997].
- Low emersion times might be less beneficial for mussel beds, because of predation of crabs and starfish.
- Sediment characteristics should not be too coarse and neither too silty because mussel larvae prefer a hard and coarse surface for settling, while adult mussels favor a more silty environment such as soft mud [McGrorty et al., 1993].
- The distance of the mussel bed to the gully, which is important because incoming flow through the gully contains nutrient for the mussels. Brinkman et al. [2002] found that an area is suitable within a maximum distance of 500 m from a gully.

Young mussels settle in dense beds that range from tens of meters up to kilometers. Mussels form aggregations in these beds in which dense patches, in which mussels form clumps that are interconnected via byssal threads, alternate with bare sediment substrate. Mutual protection from waves and currents and competition for algae are providing possible explanations for self-organization of mussels into spatial patterns (patch structures) [Van de Koppel et al., 2005]. Young mussel beds show regular spatial patterns that can be characterized with a striped pattern transverse to the dominant tidal current. These regular patterns can be destroyed during storms or fisheries, so that the mussel bed is either completely removed or irregular patterns will be formed. Another effect is that older mussels gradually lose the ability to climb upon deposited sediment and therefore tend to organize themselves in more randomly patterns. This spatial pattern formation can be considered as an important parameter for the survival chances of a mussel bed, because spatial patterning allows a mussel bed to persist higher food availability rates than a non-spatial patterned mussel bed [Van de Koppel et al., 2005].

Three patterns in mussel bed patchiness can be distinguished in the Wadden sea: uniform, striped patterns and an irregular pattern. Most of the mussel bed appear to have an irregular pattern, however 25 % of the mussel beds in the Wadden Sea can be characterized with a striped pattern transverse to the dominant current [Van de Koppel et al., 2005]. An important feature in the spatial structuring of the patches is how the flow responds to mussel patch boundaries and how the flow recovers downstream of these boundaries [Folkard and Gascoigne, 2009].

1.2 Hydrodynamic and morphological processes

Hydrodynamical processes on mussel beds have two important effects on the survival of mussels. First, the constant flow of water over the mussel bed transports

nutrients to the mussels [Widdows et al., 2002]. Second, the flowing water exerts bed shear stresses and may cause erosion of the mussel beds [Wright et al., 1997]. So it is important to understand the hydrodynamical effects on the mussel beds and conversely to study the influence of the mussel beds on the hydrodynamical process as well.

As mentioned earlier for the distance to the gully, the presence of a current is important for mussel beds because this current supplies the mussel bed with nutrients. However current velocities that are too high are less favorable, because a stronger current velocity may generate erosion of the mussel bed and prevent settlement of mussel larvae. A flume study by Widdows et al. [2002] showed that mussels need current speeds between at least 0.05 m/s and 0.8 m/s to maintain their suspension feeding. So there is sufficient vertical mixing and a relatively constant algal cell concentration in the water column on one hand and there is no detachment of the mussels on the other hand. However flume study results can deviate from field observations, because water depths and mussel bed size in the flume are restricted by the flume dimensions and wave effects are neglected. Also exhalant jets produced by mussels in the field, which enhance the amount of turbulence significantly, were not obtained in flume studies [Van Duren et al., 2006]. Most mussel beds in the Wadden Sea show maximum tidal current velocities between 0.25 m/s and 0.90 m/s, although mussel beds were also found at locations with much higher velocities up to 1.45 m/s in tidal channels [Brinkman et al., 2002]. Donker et al. [2012] showed that the location of a mussel bed may be related to wave forcing, so that wave effects should be considered as well.

1.3 Research questions

Recently effects of current velocity on a mussel patch were only studied in flume channel experiments by Folkard and Gascoigne [2009] and Lassen et al. [2006]. These experiments were performed in an environment that did not consider variable current velocities and direction and effects of waves and wind. Another deviation in these experimental setup was due to the suction due to the recirculation of the fluid in the downstream section of the flumes. So field experiments are needed to study the effects of variable current velocities and waves on the flow dynamics, shear velocity, turbulent kinetic energy and Reynolds shear stress. Likely a combination of maximum current velocity and wave exposure will affect the local hydrodynamics and result in larger shear velocities, turbulent kinetic energy and Reynolds shear stress compared to the profiles that were found by Folkard and Gascoigne [2009] and Lassen et al. [2006]. The roughness length qualifies the experienced bed shear stress due to mussels by the flow and is used to estimate shear velocities and depth averaged velocities. Therefore the roughness lengths will be determined by using the dissipation rate of turbulent kinetic energy as described by Donker et al. [2012] and compared with values from other studies (e.g. Van Duren et al. [2006] and Folkard and Gascoigne [2009]).

Another purpose of this study is to explore the effects of flow routing around a mussel patch (as will be discussed in section 2.6) which were not considered in mussel patch studies yet, since studies like Folkard and Gascoigne [2009] focused on striped

patterned mussel patches transverse to the dominant current direction. However Zong and Nepf [2010] showed that this effect is significant for a vegetation patch and therefore might be applicable for a mussel patch as well. Then measurements of a flow propagating around a mussel patch can be compared with a flow propagating over the patch. If the flow resistance is lower beside the mussel patch, flow velocities beside the mussel patch will be larger than flow velocities over the mussel patch and a wake zone with lower velocities might develop behind the downstream patch boundary. However these effects of flow routing should be weighted against the opposing effect of flow acceleration above the mussel bed due to partial blockage of the flow due to the elevation of the mussel bed with respect to its surrounding. Effects of flow acceleration due to the elevation of the mussel bed are small in case of a small elevation, so that weak flow routing effects can probably be observed.

Finally it will be important to study the effects of mussel patch boundaries in relation to flow recovery and turbulent eddy viscosity at these boundaries [Folkard and Gascoigne, 2009]. The main research questions can then be summarized as:

- What are the effects of variations in currents and waves and wind on the hydrodynamics over a mussel patch?
- Does flow routing around a mussel patch play a major role for the organization of mussels in a patch structure at this study site?
- What are the effects of mussel patch boundaries on the local hydrodynamics and can they explain advantages for the organization of mussels in a patch structure?

2 Theory

This section gives an outline of the theoretical aspects that were used to analyze hydrodynamic forces on a mussel bed. First some properties that describe a turbulent flow are explained, followed by the effects of a mussel bed with respect to the roughness height and boundary layer. Thereafter the effects of waves and wind stress on a mussel bed and its applications on the boundary layer are described and subsequently bed shear stresses due to mean currents and orbital wave motions are explained. Finally the hydrodynamic effects of an individual mussel and a mussel patch are discussed by reviewing several flume experiment results from literature.

2.1 Turbulent flow properties

Flows in the boundary layer of a sea are predominantly turbulent [Nowel and Jumars, 1984]. Turbulent flow can be characterized as a flow that undergoes irregular fluctuations on a short time scale compared to that of the forcing. While the speed of the flow is continuously changing in magnitude and direction, the main current has a specific direction [Falkovich and Sreenivasan, 2006]. The velocity components in a specific direction can be decomposed as is shown in equation 1 for the velocity component in the x-direction in, where the overbar indicates the mean (expected) velocity and the tilde and prime indicate the wave induced and turbulent fluctuations respectively [Trowbridge, 1998]:

$$u_i = \bar{u}_i + \tilde{u}_i + u'_i \quad (1)$$

Turbulence is causing vertical mixing, which provides vertical fluxes of food. Therefore turbulent eddy viscosity μ_t is a parameter of great importance for mussel beds. The effects of turbulence on vertical mixing can be taken into account by considering the turbulent kinetic energy, Reynolds shear stress or shear velocity U_{*c} [Folkard and Gascoigne, 2009].

The turbulent kinetic energy (TKE) is the mean kinetic energy per unit mass associated with eddies in turbulent flow and can be calculated by equation 2, where the over-barred terms represent the root mean squared values of the fluctuations of each velocity component u , v and w . The Reynolds shear stress component is given in equation 3, where the overbar represents the average instantaneous fluctuations of the velocity components u and w . This parameter states the rate of vertical turbulence exchange of horizontal momentum per unit volume, which is important for mussels because this regulates the vertical supply of food to them.

$$TKE = \left(\overline{u'^2} + \overline{v'^2} + \overline{w'^2} \right) \frac{1}{2} \quad (2)$$

$$\tau_{xz} = -\rho\mu_t \frac{\partial u}{\partial z} = -\overline{u'w'}\rho \quad (3)$$

where μ_t is the eddy viscosity in $Pa \cdot s$ which represents the transfer of momentum caused by turbulent eddies. Turbulent kinetic energy can be generated due to variations in bed roughness, as can be obtained in section 2.5. The generated TKE

is advected by the current and depends on the dissipation rate ϵ over time. This dissipation rate is related to the turbulence intensity which increases over rough surfaces and is large in case of strong turbulence, because of the strong mixing. On the other hand low turbulence will lead to a small dissipation rate, so that horizontal advection becomes the dominant process for this situation [Lorke et al., 2003]. So generally dissipation of TKE dominates the horizontal advection for a flow through a mussel bed, while horizontal advection of TKE dominates for a flow through smooth sediment surface away from the mussel bed.

The current related shear velocity U_{*c} and roughness height z_0 can be calculated using a method that is based on the dissipation rate of turbulent kinetic energy ϵ [Donker et al., 2012]. The production of TKE outside the wave boundary layer is assumed to be equal to the production of TKE due to bed shear stress [Tennekes and Lumley, 1972], where TKE is defined in equation 2. The turbulent kinetic energy budget is shown in equation 4, where the first left handed term is the production of TKE by current bed shear stress:

$$\overline{u'w'} \frac{\partial \bar{u}}{\partial z} - \epsilon = 0 \quad (4)$$

Based on the assumption of a balance between production and dissipation of TKE Donker et al. [2012] derived a function for the shear velocity as a function of ϵ at an elevation z above the bed:

$$U_{*c} = (\epsilon \kappa z)^{1/3} \quad (5)$$

in which κ is the Von Karman constant (≈ 0.41). Values for the TKE dissipation rate ϵ can be estimated based on sampling in the dissipation regime of the velocity spectrum $S_{ii}(\omega)$:

$$\epsilon(\omega) = \left(\frac{S_{ii}(\omega) 2(2\pi)^{3/2}}{\alpha M_{ii}(\omega)} \right) \quad (6)$$

in which the Kolmogorov constant $\alpha = 1.5$ and M_{ii} is an integral over 3D wave number space Lumley and Terray [1983] that can be calculated for every velocity component from mean flow and orbital velocities. Eventually an estimate of the roughness length z_0 can be determined as:

$$z_0 = z \exp \left(- \frac{\bar{u} \kappa^{2/3}}{(\epsilon z)^{1/3}} \right) \quad (7)$$

where \bar{u} is the time-averaged velocity component at height z .

2.2 Current boundary layer

In fully turbulent flow the vertical velocity profile has a logarithmic form, which can be described by the von Karman-Prandtl boundary layer equation (equation 8), also referred as 'law of the wall' :

$$U(z) = \frac{U_{*c}}{\kappa} \ln \frac{z}{z_0} \quad (8)$$

$$z_0 = 30k_b \quad (9)$$

Coverage	Free stream velocity (mm/s)	z_0 (mm)
Flat bottom	45	0.02
	100	0.12
	275	0.06
Mussels	55	3.5
	130	5.2
	330	4.4

Table 1: Values for roughness length z_0 by Van Duren et al. [2006]

$U(z)$ is the average flow speed (averaged over turbulent time scales) at height z above the boundary in m/s, z_0 is the hydrodynamic length scale of the surface roughness in m , k_b is the physical roughness height in m and U_{*c} is the shear velocity in m/s. The thickness of the boundary layer (δ) is defined as the height at which the fluid velocity is 99% of the free-stream velocity. The shear velocity U_{*c} is directly proportional to the bed shear stress, which is the force that is exerted on the bed by the flow, due to the flow and therefore quantifies the hydrodynamic stress that mussels experience. U_{*c} can be calculated from equation 8 if z_0 , z and $U(z)$ are known. The hydrodynamic length scale z_0 can also be determined by using an empirical relationship shown in equation 9 [Nowel and Jumars, 1984] for a hydraulically rough turbulent boundary layer in where d represents the height of the roughness elements in m . Empirical values for z_0 were determined by Van Duren et al. [2006] as shown in table 1. The current related bed shear stress $\tau_{b,c}$ (N/m^2) can be calculated as:

$$\tau_{b,c} = \rho U_{*c}^2 \quad (10)$$

The Nikuradse roughness length for a flow over a mussel bed can be calculated using the height of the roughness elements z_0 as described in the section 2.1 and then applying equation 11. For flow above fine sediment such as sand and gravel material the Nikuradse length in equation 11 is related to the grain size d_{90} (m), which is the grain diameter where 90 % of the particle has a smaller size and 10 % has a larger size. Van Leeuwen et al. [2010] proposed a roughness element size of 30 mm for a young mussel bed, however a larger roughness element size should be chosen when dealing with older and thus larger mussels.

$$k_s = \begin{cases} 3d_{90} & \text{above fine sediment} \\ 30z_0 & \text{above mussels} \end{cases} \quad (11)$$

2.3 Interaction between currents, waves and wind stress

Waves are important for mussel beds, because they generate orbital velocities that alter the flow profile and bed shear stress. These orbital velocities also cause turbulence due to the generation of turbulent eddies. This effect results in vertical mixing in the upper boundary layer of the water column, so that nutrient are transported into the benthic boundary layer. Therefore the presence of surface waves increases the uptake of nutrient by the mussels.

The near bed peak value (amplitude) of the horizontal velocity and horizontal displacement in shallow water are given in equations 12 and 13, in where h is the water depth (m), H is the wave height (m), k is the wave number (m^{-1}) defined as $k = \frac{2\pi}{L}$, ω is the wave frequency (s^{-1}) defined as $\omega = \frac{2\pi}{T}$, T is the wave period (s) and L is the wave length (m) approximated as $L = T(gh)^{0.5}$ [Van Rijn, 1990].

$$u_b = \frac{\omega H}{2 \sinh(kh)} \simeq \frac{\omega H}{2kh} \quad (12)$$

$$\hat{A}_b = \frac{H}{2 \sinh(kh)} \simeq \frac{u_b}{\omega} \quad (13)$$

These equations show that near bed orbital velocities increase as water depth decreases, but similarly a decreasing wave height decreases the orbital velocities. This effect is caused by the dissipation of wave energy at the bottom due to the generation of bed shear stress. So the orbital velocities increase when waves propagate into shallower water, but simultaneously wave energy is dissipated so that the orbital velocities decrease. The slope of the bed determines which process is dominant [De Swart and Zimmerman, 2009].

The effect of the wave generated orbital velocities near the bed results in a thinner boundary layer, because the boundary layer has no time to fully develop as velocities changes rapidly in both magnitude and direction. A typical boundary layer is in the order of centimeters above the bed. Grant and Madsen [1979] applied the effects of the wave boundary layer on the mean velocity profile outside the wave boundary layer for a combination of waves and currents by increasing the surface roughness. The mean current velocities outside the wave boundary were reduced due to wave induced turbulence by increasing the eddy viscosity in the wave boundary layer ([Grant and Madsen, 1979],[Madsen, 1994]). Donker et al. [2012] adopted this approach and formulated two equations describing the mean vertical current profiles inside and outside the wave boundary layer:

$$\bar{u}(z) = \frac{U_{*c}^2}{\kappa U_{*cw}} \ln(z/z_0) \quad z < \delta w \quad (14)$$

$$\bar{u}(z) = \frac{U_{*c}}{\kappa} \ln(z/z_{0a}) \quad z > \delta w \quad (15)$$

where z_{0a} is the apparent roughness, δw is the wave boundary layer height, U_{*c} is the current related shear velocity and U_{*cw} is the maximum shear velocity inside the wave boundary layer induced by both current and wave orbital motion. The current related shear velocity can be estimated by using equation 5 where-after the apparent roughness z_{0a} can be estimated solving equation 15. Since two unknown parameters remain in equation 14 an iterative model is required for which the Grant and Madsen wave current interaction model was used [Madsen, 1994]. This method uses a bed roughness estimate for z_0 and measurements for wave orbital velocity u_b at an elevation z above the bed, the representative peak wave period f_p and the angle between the wave and current direction. Then the model calculates new values for U_{*c} and z_{0a} using the initial estimated z_0 -value. Thereafter a new z_0 value is calculated using these new values, which is used to update z_0 until convergence is accomplished.

The wave generated maximum bed shear stress $\tau_{b,w}$ can be calculated by using equation 16 and the wave related friction factor f_w in equation 17 from Nielsen [1992].

$$\tau_{b,w} = 0.5\rho f_w (u_b)^2 \quad (16)$$

$$f_w = \exp\left(a_1 \left(\frac{u_b}{k_b 2\pi f_p}\right)^{a_2} + a_3\right) \quad (17)$$

in where f_p is the peak frequency and the empirical coefficients a_1 , a_2 and a_3 are estimated as $a_1 = 7.02$, $a_2 = -0.078$ and $a_3 = -8.82$ according to Madsen [1994]. Thereafter the total bed shear stress $\tau_{b,cw}$ is determined by a combination of the wave induced bed shear stress and current induced bed shear stress, because the interaction between the current and waves affects the vertical flow profile. The total bed shear stress can be determined using the wave current interaction model of Madsen [1994] with the obtained bed roughness height z_0 as input value, as:

$$\tau_{b,cw} = \rho U_{*cw}^2 \quad (18)$$

Interaction with wind results in a wind shear stress τ_w that is usually parameterized as:

$$\tau_w = \rho_a C_{10} U_{10}^2 \quad (19)$$

where $\rho_a = 1.25 \text{ (kg/m}^3\text{)}$ is the air density, C_{10} [-] is a drag coefficient and U_{10} is the wind speed (measured at a standard 10 m height above the surface). The drag coefficient can be solved implicitly and converges quickly after a few iterations ([Charnock, 1955];[Wüest and Lorke, 2003]):

$$C_{10} \approx [\kappa^{-1} \ln(10g/C_{10}U_{10}^2) + K]^{-2} \quad (20)$$

where K is a constant that was determined to be 11.3 ([Smith, 1988];[M.J. and Taylor, 1996]). Subsequently the wind shear stress U_{*w} at the surface is given by $\sqrt{(\tau_w/\rho)}$. The effects of of wind and wave related stress can be captured by dividing the water column in three layers: a wave-affected surface layer, a wind stress log-layer and and the current related bed-stress layer (see figure 3) [Jones and Monismith, 2008]. Each layer has a different scaling of the turbulent dissipation rate, which was described by Terray et al. [1996] as:

$$\frac{\epsilon H_s}{F} = 0.3 \left(\frac{h-z}{H_s}\right)^{-2} \quad (21)$$

where F is the estimated wind energy input that can be estimated as $F = \alpha U_{*w}^3$ with the scaling $\alpha = 54$ [Jones and Monismith, 2008]. Although this estimated α -value is specific to the measurement conditions as higher α -values were found in other studies ([Feddersen et al., 2007];[Wang and Huang, 2004]). Jones and Monismith [2008] assumed that processes like wave refraction, which result in an angle between the wind and wave directions, account for relatively small α -values, because less wind energy may be transferred to the waves if wind and wave directions are not aligned. Below the wave-affected surface layer ϵ was found to scale according to:

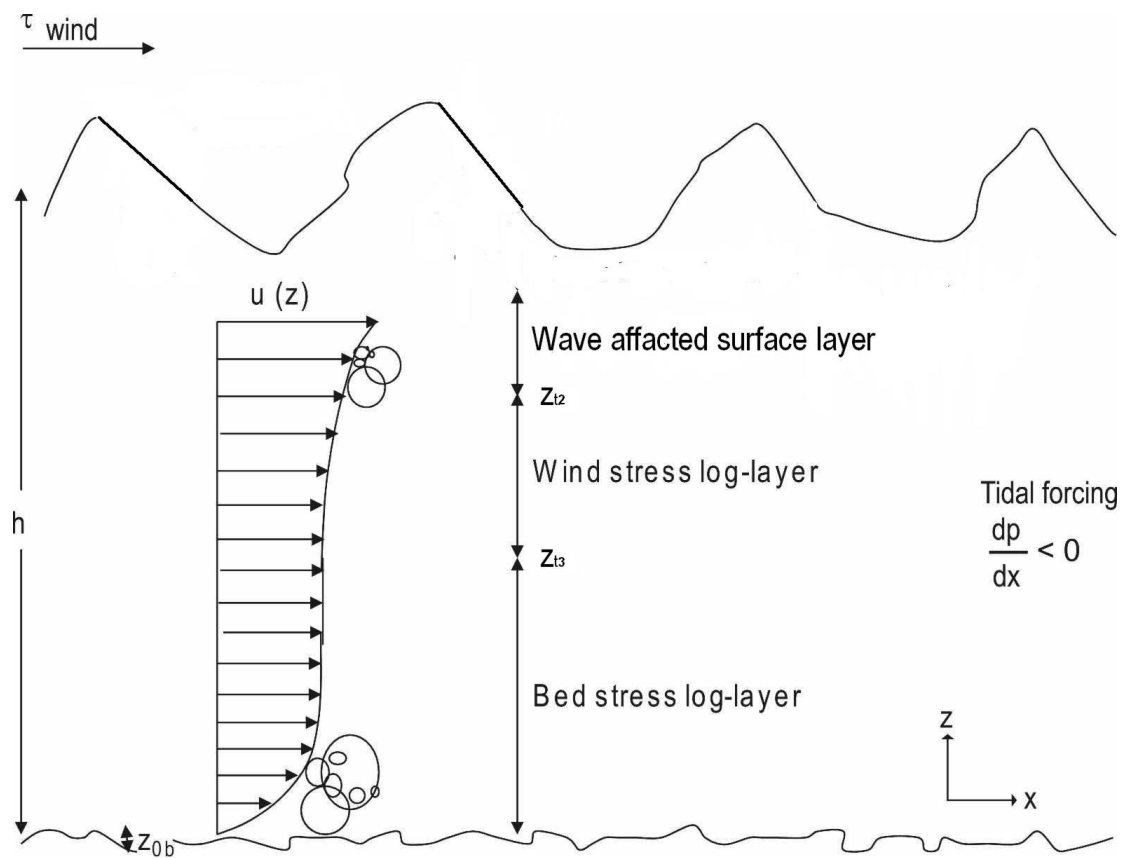


Figure 3: Schematic overview of the vertical current velocity structure of a shallow water column from combination of wind stress, waves and tidal currents [Jones and Monismith, 2008].

$$\epsilon = \frac{U_{*w}^3}{\kappa(h-z)} \quad (22)$$

In the bottom layer near the bed the turbulence is described by equation 5. To define the position of the transitions between these layers Jones and Monismith [2008] formulated equations 23-25 to define the height of the transitions. Here z_{t1} is the transition height above the bed between the wind stress log-layer and the bed shear stress layer in absence of a wave-affected surface layer:

$$z_{t1} = \frac{h}{\frac{U_{*w}^3}{U_{*b}^3} + 1} \quad (23)$$

where z_{t1} approaches h or 0 if $U_{*w} \ll U_{*b}$ or $U_{*w} \gg U_{*b}$ respectively. The height of the transition between the wave-affected surface layer and the wind stress log-layer is given by:

$$z_{t2} = h - 0.2H_s\kappa\alpha \quad (24)$$

Finally a direct transition of the wave-affected surface layer to the bed shear stress layer can be formulated as:

$$z_{t3} = \left[- \left(0.2\alpha\kappa H_s \frac{U_{*w}^3}{U_{*b}^3} + 2h \right) + \sqrt{\left(0.2\alpha\kappa H_s \frac{U_{*w}^3}{U_{*b}^3} + 2h \right)^2 - 4h^2} \right] / (-2) \quad (25)$$

Equations 23-25 can be used to predict the vertical structure of the water column and to determine the transition heights between the conditions for the conditions measured during the experiment. In cases of a well mixed water column, the wave-affected surface layer will transition directly to a bed stress log-layer ($z_{t2} < z_{t3}$).

2.4 Effects of an individual mussel and a covered mussel bed

Flume experiments by Friedrichs and Graf [2009] showed reduced horizontal velocity component U on the upstream side as well as on the downstream side of a mussel and the generation of an unstable wake region at high main flow speeds. The instability downstream of the mussel leads to increased Reynolds stresses and reduced horizontal velocities, which indicates vortex formation that increases the amount of generated turbulent kinetic energy. The vertical flow component increased on the upstream side and decreased at the downstream side of the mussel.

Like an individual mussel, a mussel bed will also affect the flow due to increased roughness near the bed and inhalant suction and exhalant jets that are produced by the mussels [Lassen et al., 2006]. Lassen et al. [2006] executed experiments to study these bed shear stresses and filtration feeding effects in which the filter feeding rates of the mussels were controlled by the supply of algal cells. Total filter feeding inactivity was succeeded by cooling of the mussels. The observed increases in TKE and Reynolds shear stress in their results in case of a maximum filtration rate indicate an increase of the biomixing. This proves that the filter feeding effects of the

mussels influence the amount of turbulent kinetic energy and bed shear stress significantly. The case of inactive filter feeding compared to the reference case of bare sand shows the effect of the increased roughness near the bed due to the structure of the mussels. The increased bed roughness is the most important effect for the generation of TKE and Reynolds shear stress, especially in case of fast flow. However filter feeding effects can not be neglected as they could even become dominant at low flow velocities. A boundary layer was developed with a length scale of approximately 70 cm (for these flow velocities) and became larger as filter feeding activity increases.

2.5 Rough to smooth surface transition

Folkard and Gascoigne [2009] performed laboratory flume experiments to study the evolution of mean flow and turbulence over and downstream of a mussel patch as well as the influence of the flow velocity to this evolution. The results show that patch-gap boundaries are very important features for the hydrodynamics over a mussel bed. Large increases in TKE, τ_{xz} and U_{*c} can be obtained, especially at the upstream edges of the patches. This behavior can be explained by the sudden changes in the mean velocity profile at these boundaries. The flow velocity in the upper part of the flow will increase at the upstream patch boundary, because the flow has to adjust itself for the partial blockage due to the elevation of the mussel bed according to conservation of mass. Simultaneously the flow experiences additional friction near the bottom due to the mussels, which causes an increase in shear stress and therefore turbulence is generated. Vertical transfer of momentum tends to restore the vertical imbalance in the flow and the gradient in flow velocity profile will decrease. A single patch experiment by Folkard and Gascoigne [2009] showed that a transition from a relatively large surface roughness to a low surface roughness will enhance an acceleration of the near-bed flow and therefore enhance turbulence.

The generation of turbulence at these rough-to-smooth (patch-gap) boundaries is important for the availability of food for the mussels, because the presence of multiple rough-to-smooth boundaries would increase the rate of nutrient transport (chlorophyll) down the water column to the mussels [Riisgard et al., 2007]. The presence of gaps leads to the restoration of near-bed nutrient rates due to the increased vertical mixing and temporary absence of losses associated with the suspension filter-feeding of the mussels [Folkard and Gascoigne, 2009]. Note that the increase of availability of nutrients for mussels is only important in areas in where the supply of nutrients is limited.

Additionally more turbulent mixing will occur in case of a larger number of patch-gap boundaries. In this case the TKE is concentrated closer to the bed, because profiles in the shorter patches have less capacity to evolve before entering the next patch-gap boundary. This might be a significantly feature for the vertical supply of nutrients to the mussels. A larger number of patch-gap boundaries results in an increased TKE and Reynolds shear stress at the end of a mussel patch section. So clearly a larger number of patch-gap boundaries is beneficial for the mussels, because increased turbulence levels result in increased vertical mixing and therefore in an increased availability of food closer to the bed combined with the recovery of food rates in the gaps.

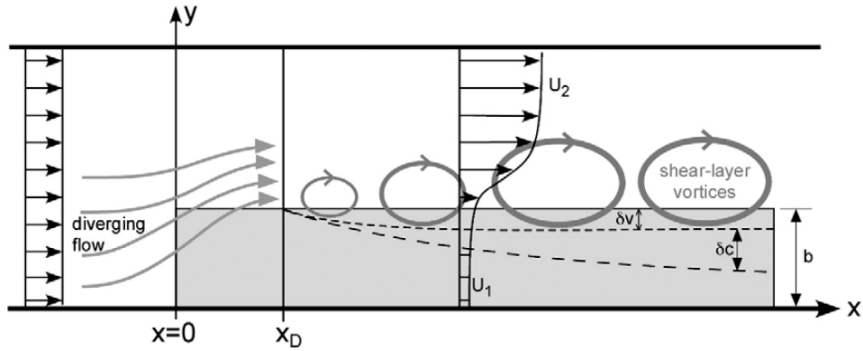


Figure 4: Schematic representation of a flow near a finite patch of vegetation (top view). Flow divergence begins upstream of the patch and extends to a distance x_D into the patch that marks the end of the diverging flow. Downstream of x_D the development of a shear-layer starts at the patch-open channel boundary. The shear-layer penetrates a distance δ_v into the patch from the patch boundary [Zong and Nepf, 2010].

2.6 Effects of flow routing

A skimming flow can be obtained if it is easier for the flow to stream around an obstacle rather than over an obstacle. This possible effect of flow routing in relation to mussel bed patches has not been considered in literature yet, however Zong and Nepf [2010] performed a flume experiment to study the flow around a finite patch of vegetation (figure 4). This setup showed a distinction into three zones. A diverging zone was obtained in the section of the channel upstream of the patch and between $x = 0$ and $x = x_D$. Behind this zone a zone arose within the vegetation where the turbulent boundary layer was fully developed. The velocity in this zone was nearly uniform across the patch width and along the length of the patch. From the same point x_D a shear layer was formed along the patch boundary which penetrated a distance δ_v into the patch. The presence of a convergent zone downstream of the patch, where reattachment of the flow is expected to occur, was not considered because of limitations in the flume length.

The height of the mussel bed does not extend through the entire boundary layer as it only reaches the lowest part of the logarithmic layer [Nowel and Jumars, 1984]. Despite the fact that the vegetation stems extend through the entire boundary layer, the results of Zong and Nepf's experiments might be applicable to characterize flow around a mussel patch. However the effects described by Zong and Nepf [2010] will be less obvious and similar experiments using a mussel patch instead of a vegetation patch should be carried out to estimate these effects. The effects of flow routing should be weighted against the effect of flow acceleration above the mussel bed due to partial blockage of the flow due to the elevation of the mussel bed with respect to its surrounding (section 2.5). In addition it will be useful to study the flow patterns downstream of the patch, because this region is important for the generation

of turbulence.

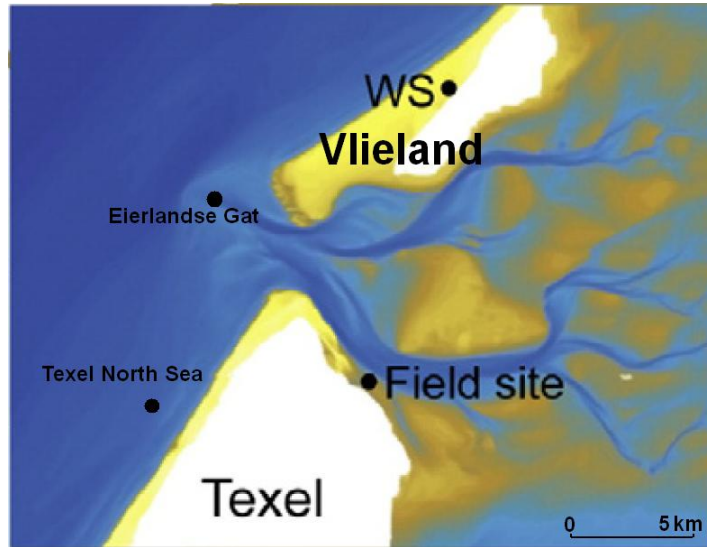


Figure 5: Measurement location with respect to barrier islands Texel and Vlieland and the location of the weather station (WS), station Eierlandse Gat and station Texel North Sea. (adjusted from Donker et al. [2012]). Morphology of the Wadden Sea is based on soundings of the Dutch ministry of Infrastructure and Environment.

3 Materials and Methods

3.1 Field location

The field experiments were performed on a mussel bed in the Wadden Sea northeast to the island of Texel in The Netherlands ($53^{\circ}9' N$, $4^{\circ}53' E$) (figure 5). The mussel bed is located close to the coastline of Texel (about 300 m), which is bordered by dikes. The mussel bed stretches from northwest to southeast over a distance of a few hundred meters. The mussel bed is protected from wind-generated waves, because waves from westerly direction break on the ebb-tidal delta. Furthermore, locally generated waves are small due to a fetch limitation caused by the shelter of Texel on the land side. Wind directions and wind speeds were obtained from a KNMI weather station on Vlieland (Dutch Royal Meteorological Institute), located approximately 13 km northeast of the field site ($53^{\circ}15' N$, $4^{\circ} 57' E$) (shown in figure 5). The dominant wind direction in the area is (south)west. Offshore wave conditions were obtained from the offshore wave buoys Texel North Sea ($53^{\circ}7' N$, $4^{\circ}44' E$) and Eierlandse Gat ($53^{\circ}16' N$, $4^{\circ}39' E$) (shown in figure 5). The tidal flat in the Wadden Sea in front of the mussel bed is sandy, while the tidal flat to the northwest is more muddy (shown at the left side in figure 6a).

The investigated mussel patch is part of this larger mussel bed and is located at the northwest side of the mussel bed and was selected because the incoming flood current can flow relatively undisturbed over the tidal flat towards the mussel patch at this location. Some oyster patches are present near the selected mussel patch and a small fraction of oysters is present inside the investigated mussel patch. The



Figure 6: Aerial photographs of the mussel bank taken in September 2011. *a)* Overview of the area, where the measurement location is marked with a red dot; *b)* Plain view of the mussel bed, where the three measurement frames are marked with colored dots and numbers.

substratum in and around the selected mussel patch showed a large spatial variation as a muddy soft substratum as well as a hard sandy substratum was found.

3.2 Equipment

Measurement instruments for obtaining wave and current characteristics were deployed in the period from the 18th of September until the 28th of October 2011. Three measurement frames were placed onto and near the mussel patch of which the locations are shown in the digital elevation map of the area in figure 10. Frame 1 contained two Acoustic Doppler Velocity (ADV) sensors (ADV type Sontek Hydra cabled version) of which the probes were orientated downward, coupled with two pressure sensors. The measurement volume of the ADV sensors was inside the frame. Also a pressure sensor type Ocean sensor systems (OSSI-010-003B Wave Gauge) was attached to a single pole of the frame. The Sontek ADVs and OSSI pressure sensor measured at a sample rate of 10 Hz.

Frame 2 contained two ADV sensors (ADV type Nortek Vector cabled version) of which the probes were orientated north (0°) for calibration purposes in the direction opposite of the dominant flood current and coupled with two pressure sensors. The sensors had different elevations above the bed and the measurement volume of the ADV sensors was in front of the frame during flood current. Measurement equipment on frame 3 had the same orientation as frame 2, but contained only a single ADV sensor (ADV type Nortek Vector cabled version) near the bed. An OSSI pressure sensor was attached to a single pole of the frames 2 and 3. The ADVs at

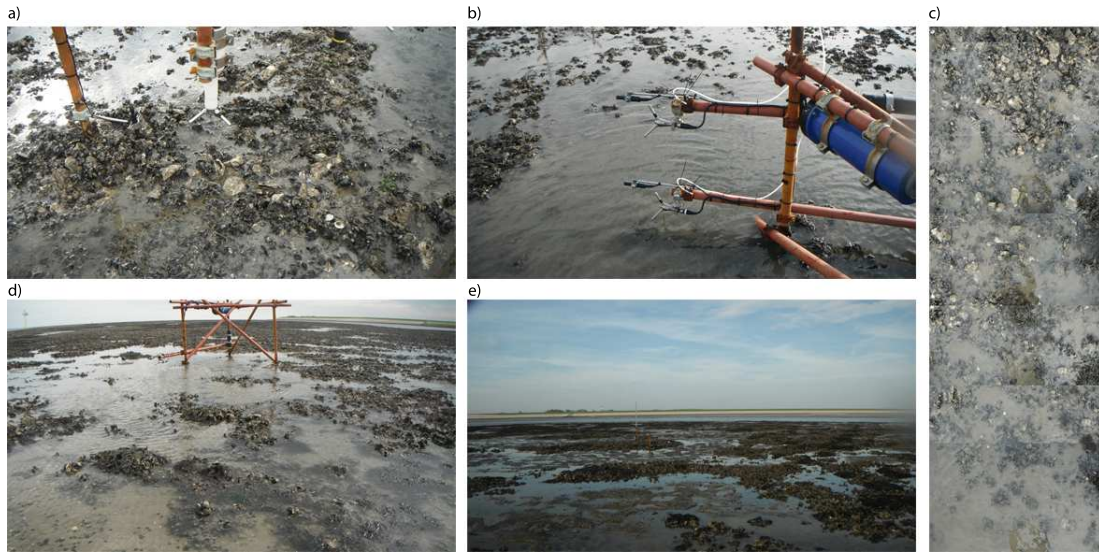


Figure 7: Overview of the position and orientation of measurement frames and ADV sensors. *a)* Detailed view of the mussel patch under the ADV sensors at frame 1; *b)* ADV sensors at frame 2; *c)* Mussel bed in front of the ADV sensors at frame 2 (about 2 meters); *d)* Position of frame 3; *e)* Oyster patches north- and westwards of frame 1.

frame 2 and 3 measured at a sample rate of 8 Hz and both OSSI pressure sensors measured at a sample rate of 10 Hz. The orientation of the ADVs in this research is defined as right-handed coordinate system: a negative u -velocity should be associated with a current that flows southwards (flood-current), a positive u -current flows northwards, a negative v -current flows eastwards and a positive current flows westwards. A positive vertical velocity component w is associated with an upward flow direction, while a negative w -component is associated with a downward flow direction (figure 8). An overview of all properties of the deployed sensors is given in table 2.

The location of the frames with respect to each other and the mussel patch is shown in the digital elevation map (figure 10). The yellow/orange spotted area between frames 1 and 2 is the location of the mussel patch of interest. Figure 7 shows a detailed view at the bed close to the ADV sensors at frame 1 and 2 and an overview of the bed in front of the ADV sensor at frame 3 and the area north- and westwards of frame 1. The ADV sensors at frame 1 are above an area that is covered by mussels, while the ADV sensors at frame 2 are located approximately 1 meter behind the mussel patch boundary above a relatively barely covered bed. Figure 7d shows that the area in front of frame 3 is relatively uncovered and contains only a small fraction of mussel coverage.

Sensor	Location	Height above bed (m)	Height above NAP (m)	Frequency (Hz)	Orientation
Ossi 1	frame 1	0.13	-0.07	10	down
Ossi 2	frame 2	0.11	-0.09	10	down
Ossi 3	frame 3	0.20	-0.07	10	down
ADV 1	frame 2	0.14	-0.07	8	North
ADV 2	frame 2	0.61	0.40	8	North
ADV 3	frame 3	0.12	-0.09	8	North
ADV 4	frame 1	0.12	-0.13	10	down
ADV 5	frame 1	0.62	0.38	10	down
ADV pressure 1	frame 1	0.82	0.58	10	down
ADV pressure 2	frame 2	0.80	0.60	8	down
ADV pressure 3	frame 3	1.01	0.80	8	down

Table 2: Properties of deployed sensors

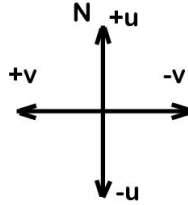


Figure 8: Definition sketch of ADV sensor orientation (plan view) showing a right-handed coordinate system. A negative u -component is defined to flow to the south, a positive component to the north, a negative v -component to the east and a positive v -component to the west. Additionally a positive vertical velocity component w is associated with an upward flow direction, while a negative w -component is associated with a downward flow direction

3.3 Data processing

Time series that were collected from the ADV sensors were cleaned in data blocks with a length of 1 minute by removing outliers from the data. Time series have been checked for outliers based on the signal to noise ratio (SNR), correlation ratio and spike noise. Data points were removed if the SNR was smaller than the SNR threshold, where SNR threshold values were 8 and 100 for the Nortek and Sontek ADVs respectively. Outliers based on correlation were removed if correlation was smaller than the correlation threshold, where the correlation threshold was computed by:

$$\text{corthreshold} = 30 + 40\sqrt{fs/fs_{max}} \quad (26)$$

in which fs_{max} is the maximum sample frequency in Herz, which was 32 and 25 Hz for the Nortek and Sontek ADV respectively and fs is the sample frequency in Herz. Spike noise was removed from the data by using the phase-space method by Goring and Nikora [2002] in which an ellipsoid is constructed in three-dimensional phase space and points outside this ellipsoid are characterized as spikes. Removed data was replaced with spline interpolated data in case less than 1% of the data in a block was removed, else all data in the block was rejected. Subsequently the cleaned beams of the Nortek ADVs were multiplied with a transformation matrix to transform the direction of the beams into an u,v,w -coordinate system. The beams of the Sontek ADV were already orientated in this coordinate system.

Time series that were collected from the Ossi pressure sensors were corrected for air pressure and converted to sea surface elevation by linear wave theory. Thereafter the signal was detrended and corrected for depth-attenuation of pressure to obtain the mean water depth. This water depth time series was split into 1 minutes records, which were rejected if a record contained more than 1% missing data. Subsequently the Welch power spectrum $S_{p,j}$, where j is the frequency component, was calculated using a 52 s window with 50% overlap and this spectrum was logarithmically averaged into frequency bands. The transformation of the pressure power spectrum into the surface elevation power spectrum follows from linear wave theory:

$$S_{w,j} = \left(\frac{\cosh(k_j h)}{\rho g \cosh(k_j (h - z))} \right)^2 S_{p,j} \quad (27)$$

Finally the root mean squared wave height is calculated by bandwidth averaging of the wave height of each frequency component:

$$H_{rms} = \sqrt{8} \left(\sum_{j=1}^N S_{w,j} \Delta f \right)^{1/2} \quad (28)$$

in which Δf is the frequency bandwidth in Hz.

The velocity surface elevation spectra were computed using the same method, but now the velocity data of the ADV's is used instead of the pressure data. These velocity based surface elevation spectra were used to determine the mean wave angle and spreading, which are energy weighted average values that were calculated according to [Herbers et al., 1999] and [Henderson et al., 2006]. This method uses the orientation of the dominant principal axis of the covariance matrix of u and v for

the mean wave angle and the square root of the ratio between the velocity variance perpendicular to this dominant axis and total variance for the mean wave spreading.

Calculations of the turbulent kinetic energy and Reynolds stress were done according to the methods described by Feddersen and Williams [2007] and Trowbridge [1998]. The sensor separation should be sufficiently large so that the separation is small with respect to the wavelength, but large with respect to the turbulence length scale. Then the wave bias is removed and the corrected velocity only contains turbulence components. Feddersen and Williams [2007] estimated the Reynolds stress from the velocity difference in u - and w -direction between two vertically separated ADV sensors, taking a small angle between the sensors into account. The advantage of their method is that wave velocity magnitude variations and phase shift that can lead to large differenced wave velocities are reduced due to an adaptive filtering technique. Eventually the differenced velocities were averaged over a period of 10 minutes and used to calculate the Reynolds stresses and TKE using equations 2 and 3. Here $\overline{u'w'}$ is calculated as covariance of the filtered differenced velocities $\Delta\hat{u}$ and $\Delta\hat{w}$ by:

$$\overline{u'w'} = cov(\overline{\Delta\hat{u}}, \overline{\Delta\hat{w}}) \quad (29)$$

Feddersen and Williams [2007] 's method may be expanded so that the pressure signal of the internal ADV and Ossi pressure sensors can be used as correlation signal instead of the upper velocity signal, which is particularly useful to compute estimates of Reynolds stresses and TKE at measurement locations that contain a single ADV sensor. This method is based on the correlation between the pressure sensor time series and the ADV sensor time series. The variations in pressure can be assigned to variations in the water level and wave height, which is related to orbital velocities. Therefore the pressure signal could give a reasonable estimate of the upper velocity fluctuations. To adjust for deviations between Feddersen and Williams [2007] 's method and this pressure correction method that might occur because the upper velocity signal and the pressure signal are not exactly correlated, linear regression yields coefficients a and b such that $\overline{u'w'} = a \cdot cov(\overline{\Delta\hat{u}}, \overline{\Delta\hat{w}}) + b$. These coefficients and total errors can qualify the validity of the internal ADV and Ossi pressure correction methods with respect to the original ADV velocity correction method.

The rate of turbulent kinetic energy dissipation ϵ was estimated with a model for wave effects on the turbulent spectrum [Lumley and Terray, 1983] along with the observed velocity frequency spectrum. The turbulent velocity fluctuations induced variance is estimated by fitting this model spectrum to the observed spectra. The method of Gerbi et al. [2009] was used for this estimation, which is an optimized version of the original approach by Feddersen and Williams [2007]. The dissipation rate is computed in the turbulent inertial-subrange in the frequency range of [1.5-3] Hz and the frequency noise range is [4-5] Hz . The dissipation rates were verified with a quality-control method by Feddersen [2010]. First this method checks if the frequency dependence of the u , v and w velocity spectra equal $f^{-5/3}$, which is the theoretical slope of the inertial subrange in fully developed turbulence. The second check is to test if the ratio R , between the horizontal and vertical velocity spectra, is between 0.5 and 2 in the inertial subrange.

Day	Date	Wind speed (m/s)	Wind direction	Wave height (m)	Wave direction	U_{max} (m/s)	Tidal elevation(m)
15	10/01	1-3	variable	very low	north-northeast	average	average
32	10/18	10-15	west	low	north-northeast	high	high
38	10/24	10-12	southeast	low	east	low	very low

Table 3: Environmental conditions on selected days at the measurement site

3.4 Bed level

The elevation of the mussel bed and surrounding area was measured by using a dGPS device (TRIMBLE GNSS ROVER). The measurement points were taken close to each other on and near the mussel patch, while the point coverage is less dense further away from the mussel patch (figure 10). A digital elevation map of the covered area was created by using the natural neighbor interpolation method. Earlier research in this area [Donker et al., 2012] showed that the elevation of the area can be considered as constant over the measurement period of 1.5 months. The aerial photographs (figure 6) were taken just before the measurement period in September 2011.

3.5 Environmental conditions

Environmental conditions (wind speed and direction, wave height and direction, water levels and current velocities) over the entire measurement period are shown in figure 9. The wind speed and direction were measured at the nearby KNMI (Royal Dutch Meteorological Institute) weather station Vlieland (see figure 5). The wave height and direction were measured at station Eierlandse Gat of Rijkswaterstaat (Part of Dutch ministry of public works) and at the site (at frame 2). The water level was measured at station Texel North Sea and at the site (at frame 2) and the current velocities were measured at the site at frame 2 (figure 5).

3.6 Data selection

To study the hydrodynamic effects of the mussel patch a selection of three days was made using the environmental conditions (wind speed and direction, wave height and direction, water levels and current velocities) over the entire measurement period as shown in figure 9. A period of low wind exposure from various directions was measured at day 15 (01-10-2011), at which the wind speeds were 1-3 m/s . The wave height at both station Eierlandse Gat (from a northwestern direction) and site (from northern/northeastern direction) are very low. Therefore day 15 provided adequate calm wave conditions for studying effects of current velocities on the mussel patch. A stormy period was measured at day 32 (18-10-2011) with a western wind direction with wind speeds of 10-15 m/s . High wave heights at station Eierlandse Gat from western to northwestern directions were obtained during this period, however the northern/northeastern wave direction at the site is similar to day 15. So day 32 provided similar conditions as day 15 except much higher wind speeds and wave

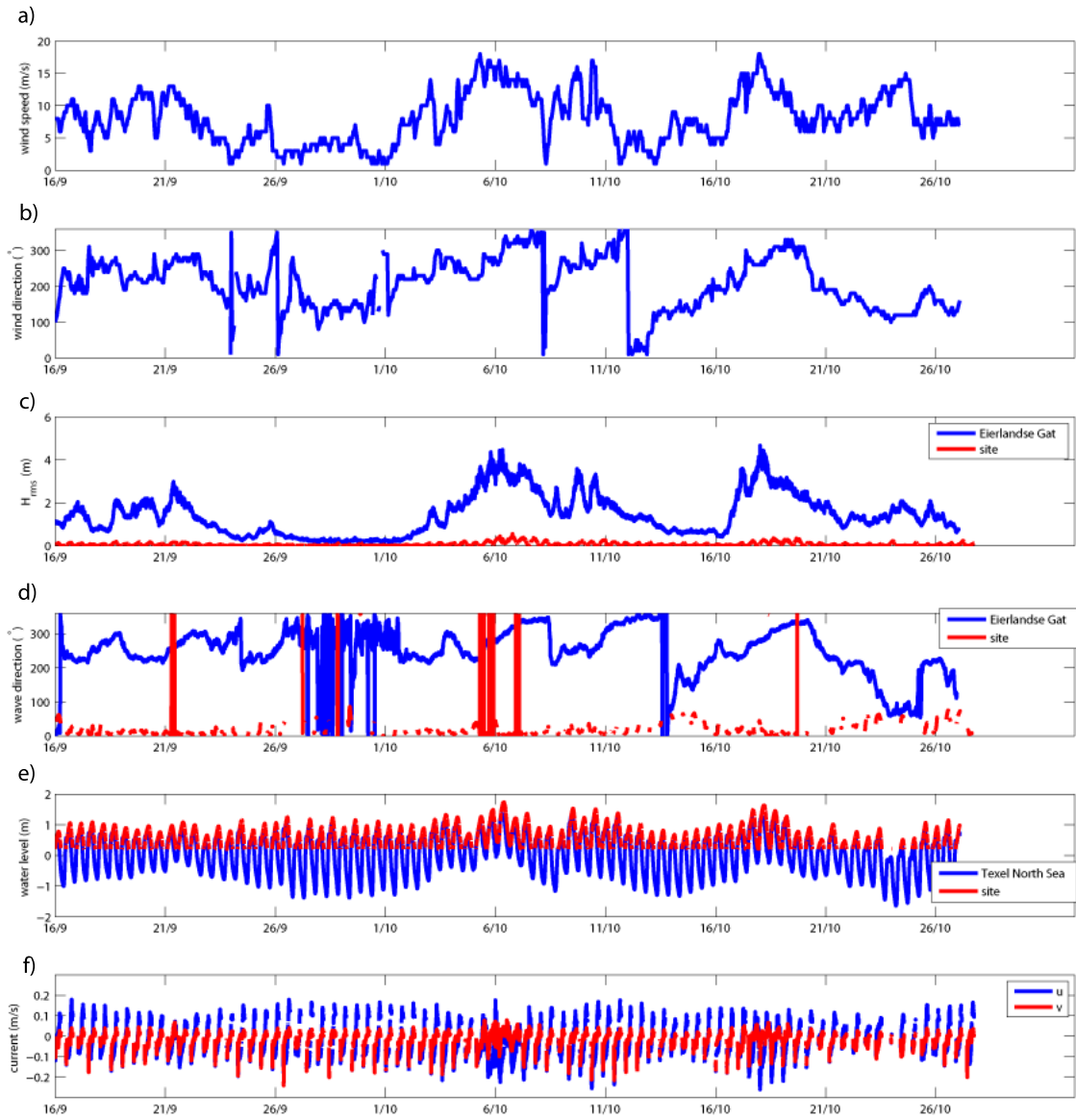


Figure 9: *a)* Wind speed (m/s) and *b)* direction ($^{\circ}$) at KNMI station Vlieland; *c)* H_{rms} (m) at station Eierlandse Gat and at the site (frame 2); wave direction ($^{\circ}$) at station Eierlandse Gat; *d)* wave direction at field site; *e)* water level (m) with respect to NAP at station Texel North Sea and water depth (m) at site (frame 2); *f)* u - and v -current velocities (m/s) at the site (frame 2)

heights at the North Sea and therefore day 32 was used to study these additional effects on current velocities on the mussel patch. Finally a period of high wind speeds of 10-12 m/s from a southeastern direction was measured at day 38. A different wave direction was measured during this period as waves in the North Sea and at the site propagate from an eastern direction. Therefore day 38 provided alternative conditions that might have different effects on current velocities on the mussel patch.

4 Results

4.1 Bathymetry

The bathymetry of the area was measured with dGPS point measurements. In the mussel patch area the distance between sample points was about 10 cm, so that a very detailed digital elevation map was computed. The mussel patch can be recognized in the elevation map (figure 10a) by the higher elevated areas (orange/yellow spots) between frame 1 and 2. The elevation of the mussel patch with respect to its surrounding is about 10 cm, however elevation differences can rise to 20 cm towards the gully eastward of the mussel patch. Peaks in height near the investigated mussel patch, which are predominantly northwards of the patch, are attributed to oysters. The map of the elevation in the surrounding area (figure 10b) shows an overview of the area between the investigated mussel patch towards the tidal channel and was computed with a courser measurement point density (about 2 meters spacing). This figure shows the presence of a higher elevated area between the investigated mussel patch and the tidal channel, which protects the mussel patch to waves from a NE direction.

4.2 Tidal characteristics

The water levels of the selected days are plotted in figure 11. Water levels on 18/10 and 24/10 can be characterized as respectively spring and neap tide (figure 5). The setup and setdown of the water levels correspond with a maximum water level on 18/10 of 1.0 *m*, while the maximum water level on 24/10 was only 0.6 *m*. Water levels on 01/10 were characterized as average tide. The weak tide on 24/10 caused a lower submersion time of the mussel patch and therefore the graph in figure 11 is missing the first and last part of the tidal cycle on this day. Analysis of the water depth curves shows a steep gradient in the initial phase of the flood period, whereafter the gradient becomes less steep towards slack tide. However this steep gradient in the initial phase of the flood period is missing on 24/10, because the wind conditions on this day result in lower water levels in the Wadden Sea. Also note that the duration of the falling tide is shorter than the rising tide, so that the water levels rise more slowly than they fall.

Tidal currents were characterized by plotting velocity vectors (averaged over a 30 minutes period) for the tidal periods of the selected days (figure 12). The orientation and length of the vector arrows correspond with the direction of the mean current and magnitude of the mean current respectively. This velocity vector plot shows that the mean currents were aligned along the north-south axis during most of the tidal cycle, meaning that the *v*-component of the current is relatively small compared to the *u*-component. A deviation in the magnitude and direction of the currents was obtained after an hour during the flood current. Increased velocity magnitudes of 0.20 and 0.21 *m/s* were obtained in this period on 01/10 and 18/10 respectively, while the direction of the mean current was more easterly. However this variation in the velocity vector plot was not obtained for the different environmental conditions on 24/10, where mean currents were smaller and orientated more easterly during the flood current than on 01/10 and 18/10. This current velocity peak might be caused by an accumulation of water on a tidal flat, followed by a quick draining if a specific

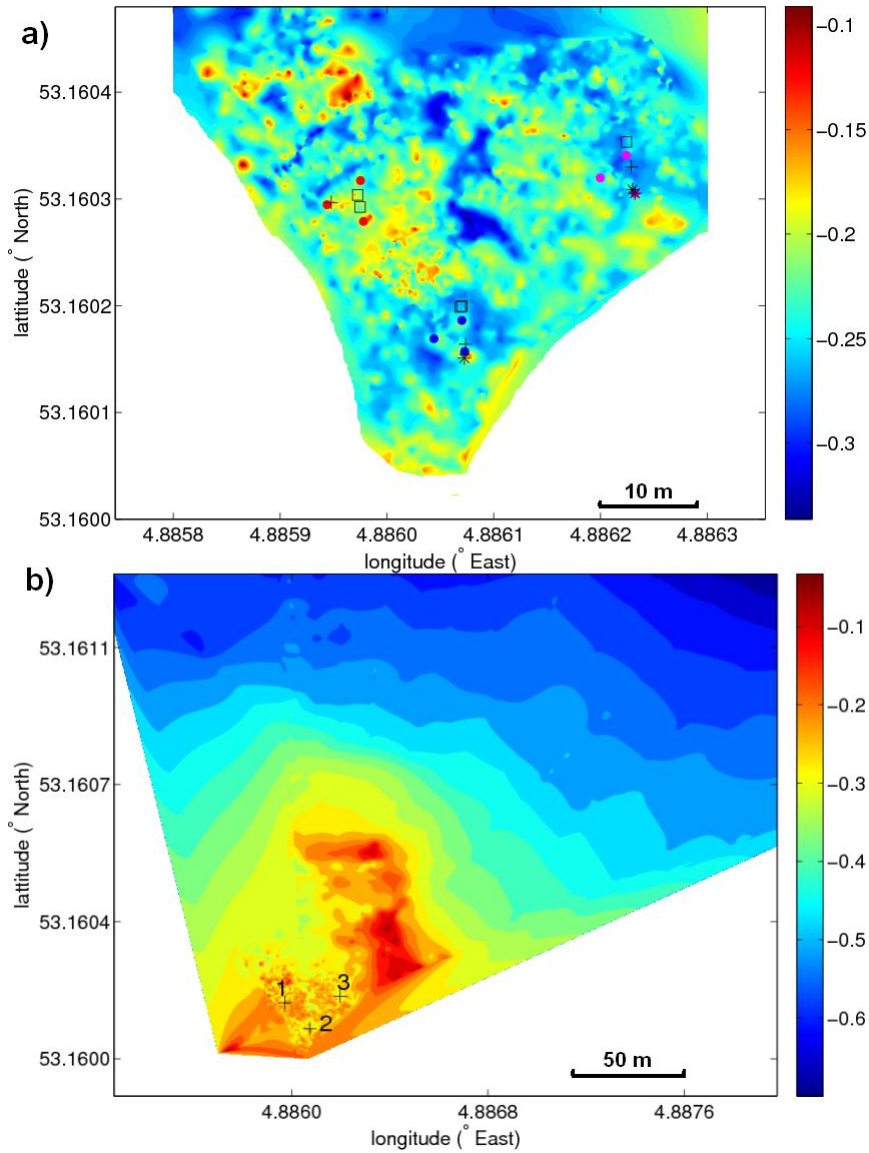


Figure 10: *a)* Digital elevation map of the mussel patch area and surroundings showing positions of measurement frames, ADV sensors and pressure sensors. The red dots indicate the poles of frame 1, blue dots are frame 2 and magenta dots are frame 3. The rectangles show the positions of the ADV sensors, where the northern sensor at frame 1 corresponds with the lower ADV sensor and the southern sensor corresponds with the upper ADV sensor. The stars show the OSSI pressure sensor locations, while the plus-signs indicate the locations of the Nortek pressure sensors. *b)* Digital elevation map of the mussel patch area and surroundings. The number indicate the measurement locations (frames 1, 2 and 3). The colorbars in both figures represent the elevation in meters above NAP (mean sea level) and coordinates are shown in WGS84.

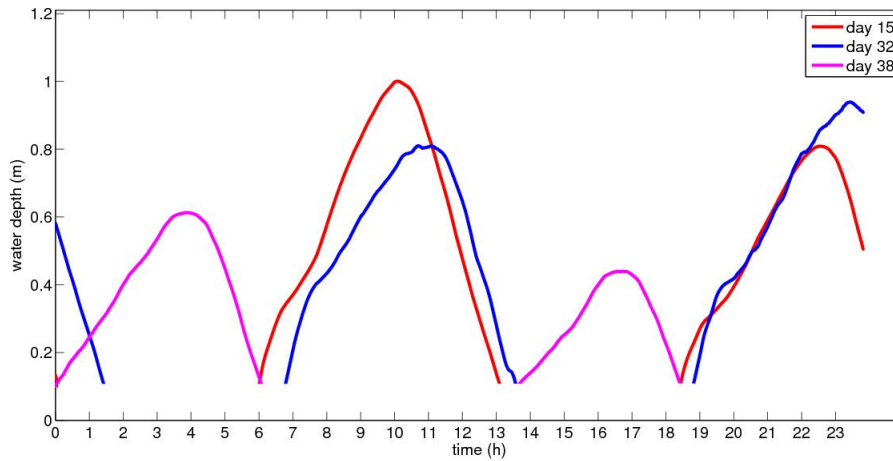


Figure 11: Water depths at site (obtained from pressure sensor on frame 3) above the threshold of 0.1 m at day 15, 32 and 38 as a function of time in hours at the specific day.

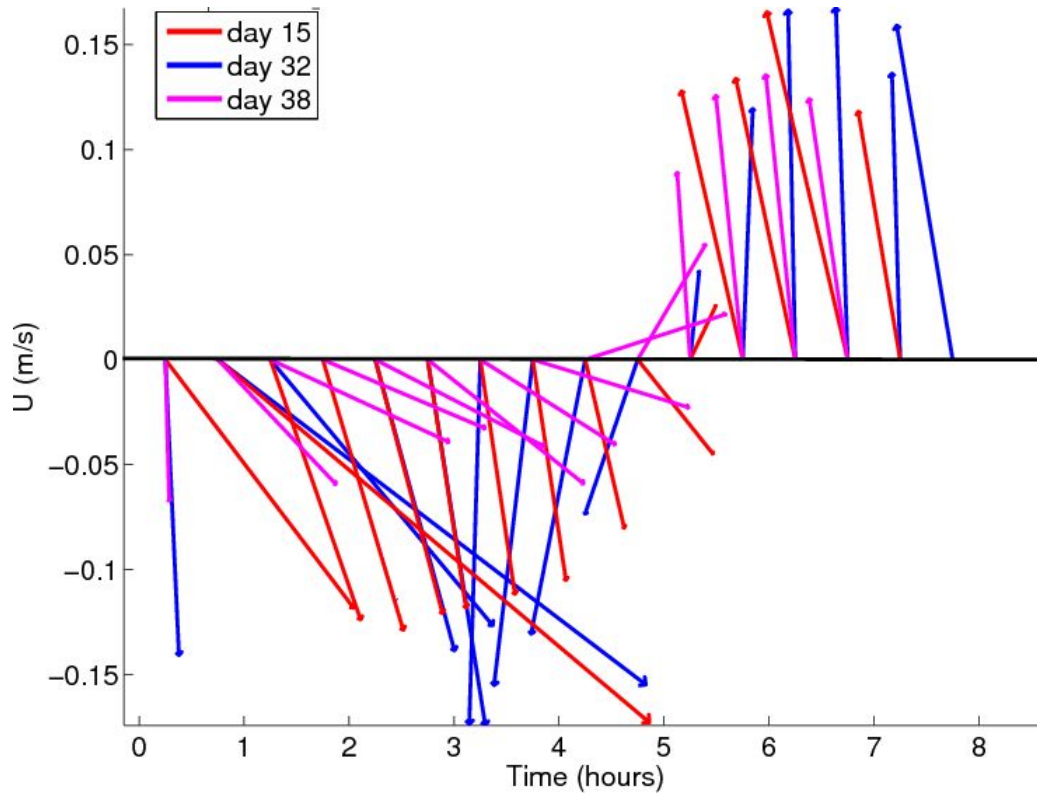


Figure 12: Magnitude and direction of current velocities at site (obtained from ADV on frame 3) at day 15, 32 and 38 as a function of time in hours at the specific day for 1 tidal cycle. $t = 0$ is defined as the start of the tidal cycle at which a first ADV signal was obtained.

water level is reached. Different conditions on 24/10 possibly prevent this pattern. The ebb-currents were dominated by the u -component of the mean current, while a small v -components was obtained in a westerly direction. Unlike the flood current, the ebb current magnitudes and directions were relatively constant over all selected days. This indicates that different mechanisms are important for the flood and ebb currents as ebb current is more dominated by (small) tidal channels compared to the flood current.

A more detailed analysis of the tidal characteristics of the mussel bed area is obtained by plotting the u -component of the current velocity as a function of the v -component and by plotting the magnitude of the current velocity U as a function of the water depth h (figure 13). The axes of the scatterplots were set to the orientation of the ADVs, so the x-axis is the north-south axis and the y-axis is the west-east axis. A distinctive peak in the u - and v -currents, both in negative direction (so directed towards the southeast), can be distinguished on 01/10 and 18/10 (figures 13a,c). However this distinctive peak was not obtained on 24/10 (figure 13e). These maximum current velocities were observed in combination with a relatively low water level around 0.5 m in the initial phase of the flood period (figure 12). The remaining flood period showed relatively small negative v -currents compared to the negative u -current on 01/10 and 18/10, which shows that the u -current is the main tidal current component for flow over the mussel patch from frame 1 to frame 2. However a different pattern was obtained on 24/10, where figure 13e shows relatively large v -currents and relatively small u -currents compared to currents on 01/10 and 18/10. This different tidal current ellipse on 24/10 is related to lower water levels during this tidal cycle, therefore surrounding tidal flats and the mussel bed became submerged at a later time in the tidal cycle so that the peak velocity in the initial phase of the flood period that was obtained on 01/10 and 18/10 is missing on 24/10. Note that a part of the ellipsoids in figure 13 are missing, because the ADVs cannot measure currents during low water depths (ADV sensors were emerged).

4.3 Current velocities

The current velocities on the mussel patch near the upstream patch boundary, behind the downstream patch boundary and beside the patch at respectively frames 1, 2 and 3 on 01/10 are plotted in figure 14. Similar plots for 18/10 and 24/10 are shown in figures 16 and 18. Note that a negative u -current corresponds with a flood current that flows from north to south and a positive u -current corresponds with an ebb-current that flows from south to north. Likewise a negative v -current flows from east to west, while a positive v -current flows from west to east (see figure 8). A positive w -current corresponds with a flow in an upward direction, while a negative w -current corresponds with a flow in a downward direction. The current related shear velocity U_{*c} was determined using equation 8 and depth average current velocities were computed by integrating this equation over the elevation above the bed (z). Roughness lengths ($z_0 = 30k_b$) were determined using k_b -values from table 6.

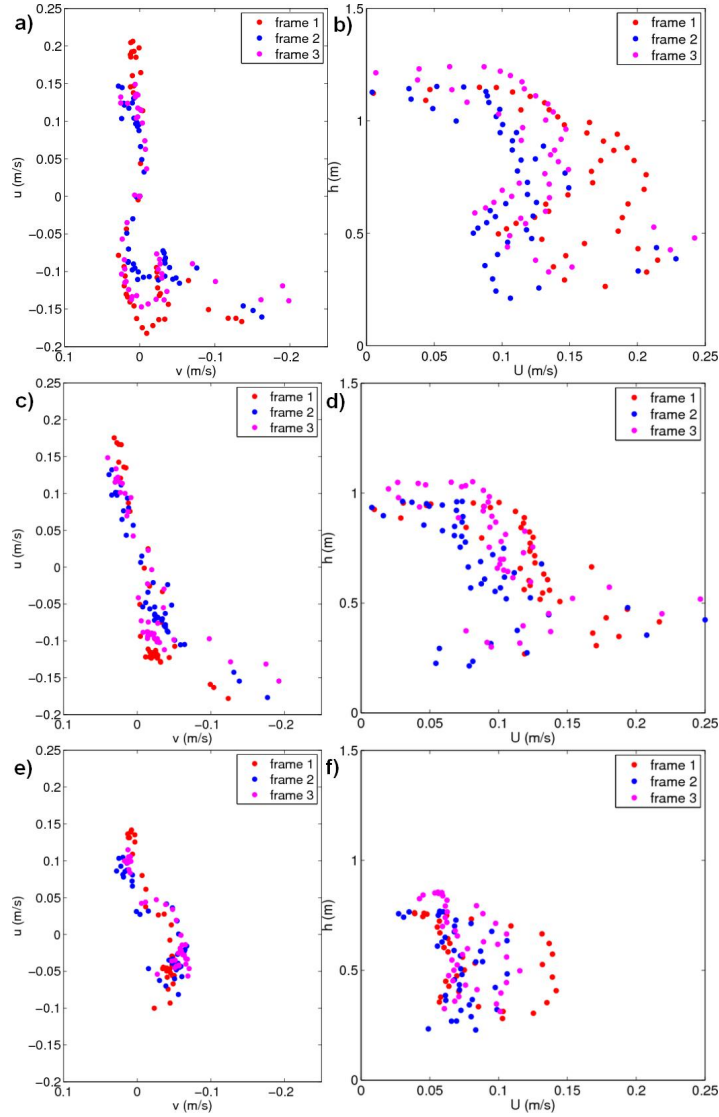


Figure 13: Scatter plots of current velocity ellipses (10 minutes averaged values of u and v) for all frames on *a*) 01/10, *c*) 18/10 and *e*) 24/10 and scatter plots of the current velocity magnitude as a function of the water depth h for all frames on *b*) 01/10, *d*) 18/10 and *f*) 24/10. All data was obtained from the lower ADVs and pressure sensors.

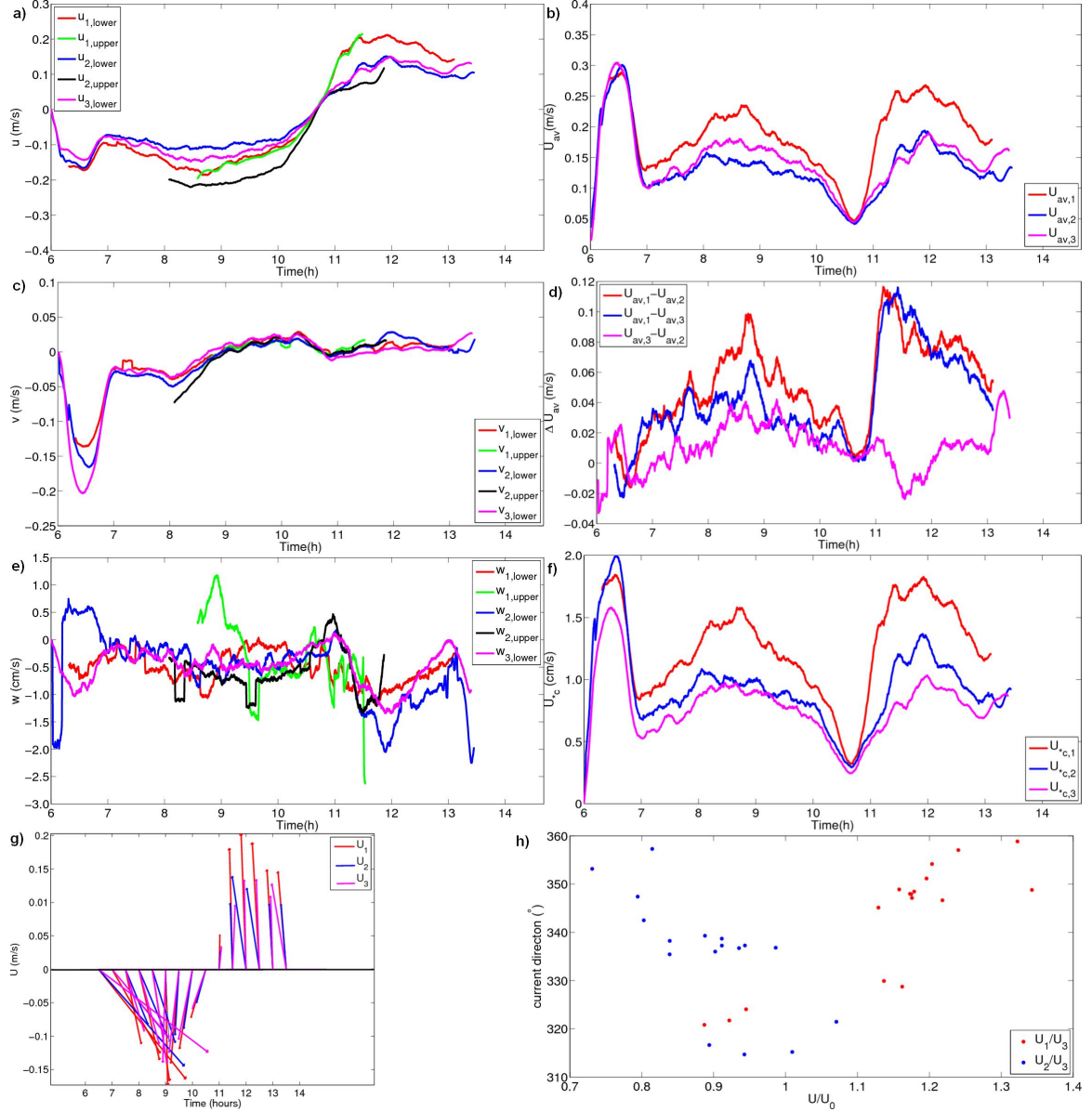


Figure 14: All panels show 10 minutes moving averaged values on 01/10 for all measurement locations. The subscripts denote the measurement location with numbers and the sensor position near the bed or away from the bed by lower and upper. *a)* Current velocity u ; *b)* Current velocity v ; *c)* Current velocity w ; *d)* Depth average current velocity; *e)* Difference of depth average current velocities between measurement locations; *f)* Current related shear velocity U_{*c} ; *g)* Current velocity vectors indicating the magnitude and direction of the flow (30 minute averages); *h)* Scaled current velocity as a function of the current direction. Current velocities at frames 1 and 2 are scaled by the free stream velocity U_3 .

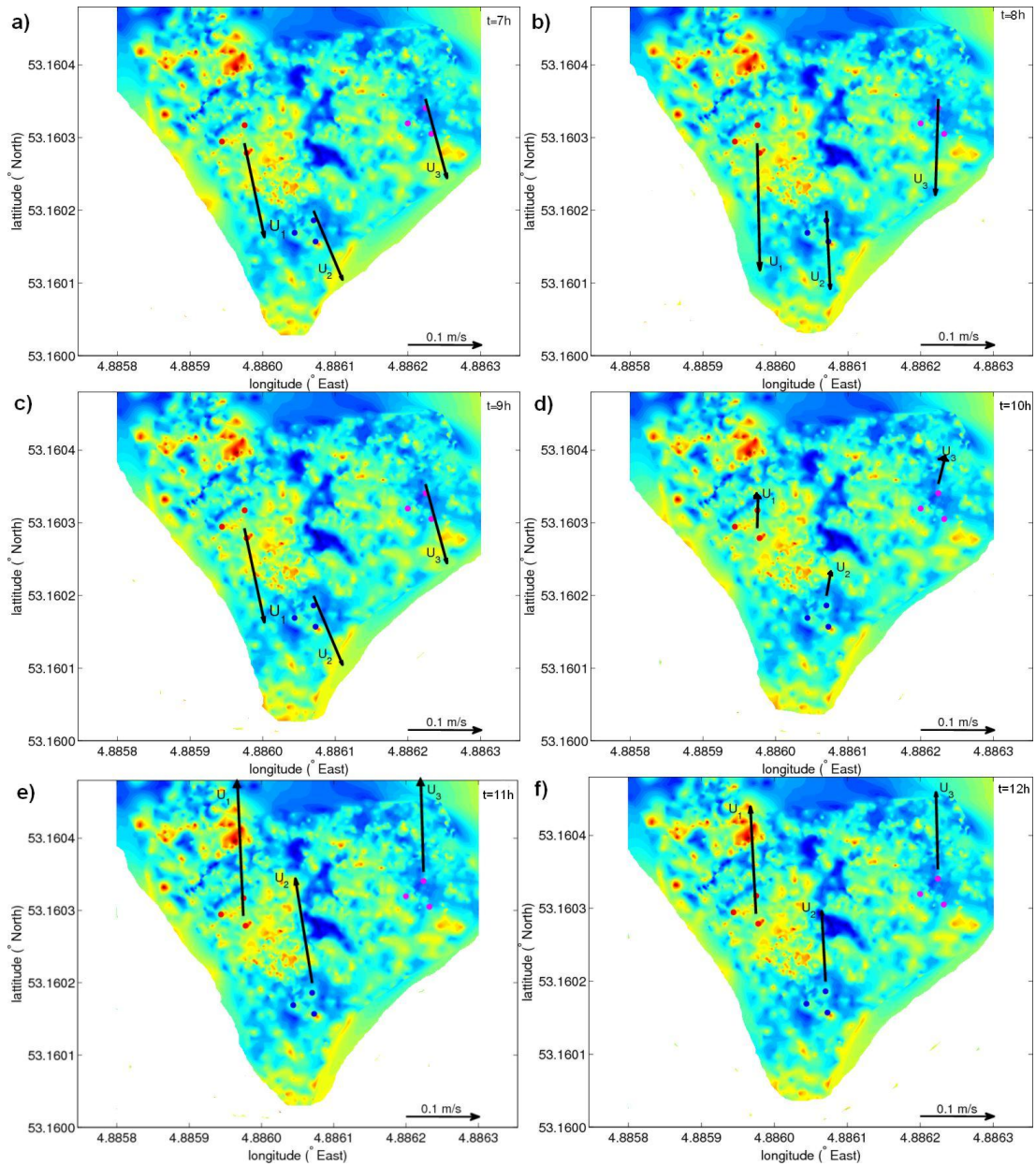


Figure 15: Overview of the magnitude and direction of the near bed currents on the measurement locations on and near the mussel patch with underlying bathymetry on 01/10. The vector arrows show the average current velocity U magnitude and direction of the previous 10 minutes at 6 moments during the tidal cycle using equal scales for the north-south and east-west components. The subscript numbers indicate the measurement location and the colored dots indicate the positions of the measurement frame poles.

4.3.1 Tide-dominated current with low wind exposure

The current velocities u and v in figure 14a and 14b on 01/10 show a distinctive peak in the u - and v -current in the initial phase of flood between $t = 6h$ and $t = 7h$, which was already noticed in the tidal ellipsoid analysis. The magnitude of the depth average current velocity is the same for all measurement frames, but in the v -component is relatively high at frame 3 with respect to frames 1 and 2 so that the current had a more eastern direction at frame 3. These peak velocities generated high shear velocities as well, which were highest at frame 2. v -currents were relatively low during the rest of the tide and therefore currents were dominated by the u -component, which means that the main flow direction was along the north-south axis. Plots of depth average current velocity magnitude and difference between the measurement locations (figure 14b,d) show that the current velocities at frame 1 were higher than at frames 2 and 3 during both flood and ebb. The effects of flow over the mussel patch and alongside the mussel patch can be studied by comparing the current velocities at frame 2 and 3. After the initial phase of the flood a higher current velocity U_{av} was observed at frame 3 with respect to frame 2 during flood, while the current velocities were similar during ebb. This is illustrated by the magenta line in figure 14d which shows a slightly positive value. The combination of lower depth average velocities and higher shear velocities at frame 2 indicates that the flow lost more energy through flowing over the mussel patch than through flowing along the patch. However there is no direct evidence for flow routing, since current velocities were significantly lower at frame 3 compared with frame 1 so that the flow decelerated also along the patch. But lower currents at frame 2 could also be observed if frame 2 would be in the wake zone of the mussel patch due to flow routing around the patch. An overview of the current velocities on the measurement locations is shown in figure 15 at six periods during the tidal cycle.

4.3.2 Average tide with high wind exposure from a southwestern direction

A similar peak in the current velocity as on 01/10 for tide-dominated conditions was obtained in the first hour of the flood period on 18/10 (figures 16a and 16b). During the remainder of the tidal period a series of local minima and maxima occurred in the current velocities at all measurement locations and these local minima and maxima were clearly observed in both u -currents and v -currents at all measurement locations and both near the bed and away from the bed. This periodic behavior is studied in more detail in section 4.3.4. The remainder of the tidal cycle shows that current velocities were highest at frame 1, while current velocities were decreasing when both traveling over the patch and beside the mussel patch. A small v -current with respect to the u -current resulted in a current direction towards the south-southeast and the north-northwest during respectively flood and ebb. Plots of depth average current velocity magnitude and difference between the measurement locations (figure 16b,d) show that the current velocities at frame 1 were higher than at frames 2 and 3 during both flood and ebb. Similar to the conditions on 01/10, a higher current velocity U_{av} was observed on 18/10 at frame 3 with respect to frame 2 during flood. The combination of these lower depth average current velocities and higher shear velocities during flood at frame 2 with respect to frame 3 gives the same indi-

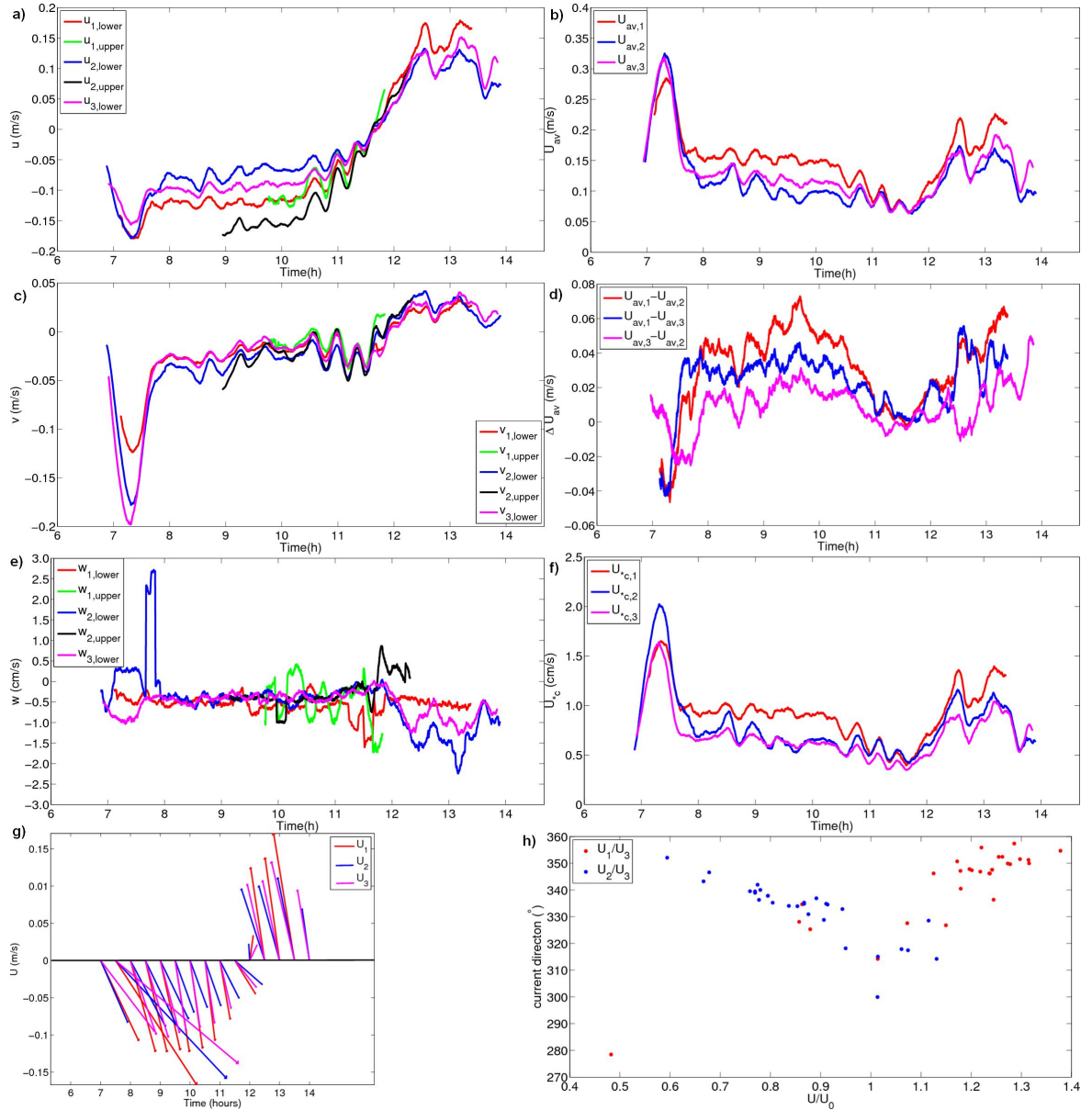


Figure 16: All panels show 10 minutes moving averaged values on 18/10 for all measurement locations. The subscripts denote the measurement location with numbers and the sensor position near the bed or away from the bed by lower and upper. *a)* Current velocity u ; *b)* Current velocity v ; *c)* Current velocity w ; *d)* Depth average current velocity; *e)* Difference of depth average current velocities between measurement locations; *f)* Current related shear velocity U_{*c} ; *g)* Current velocity vectors indicating the magnitude and direction of the flow (30 minute averages); *h)* Scaled current velocity as a function of the current direction. Current velocities at frames 1 and 2 are scaled by the free stream velocity U_3 .

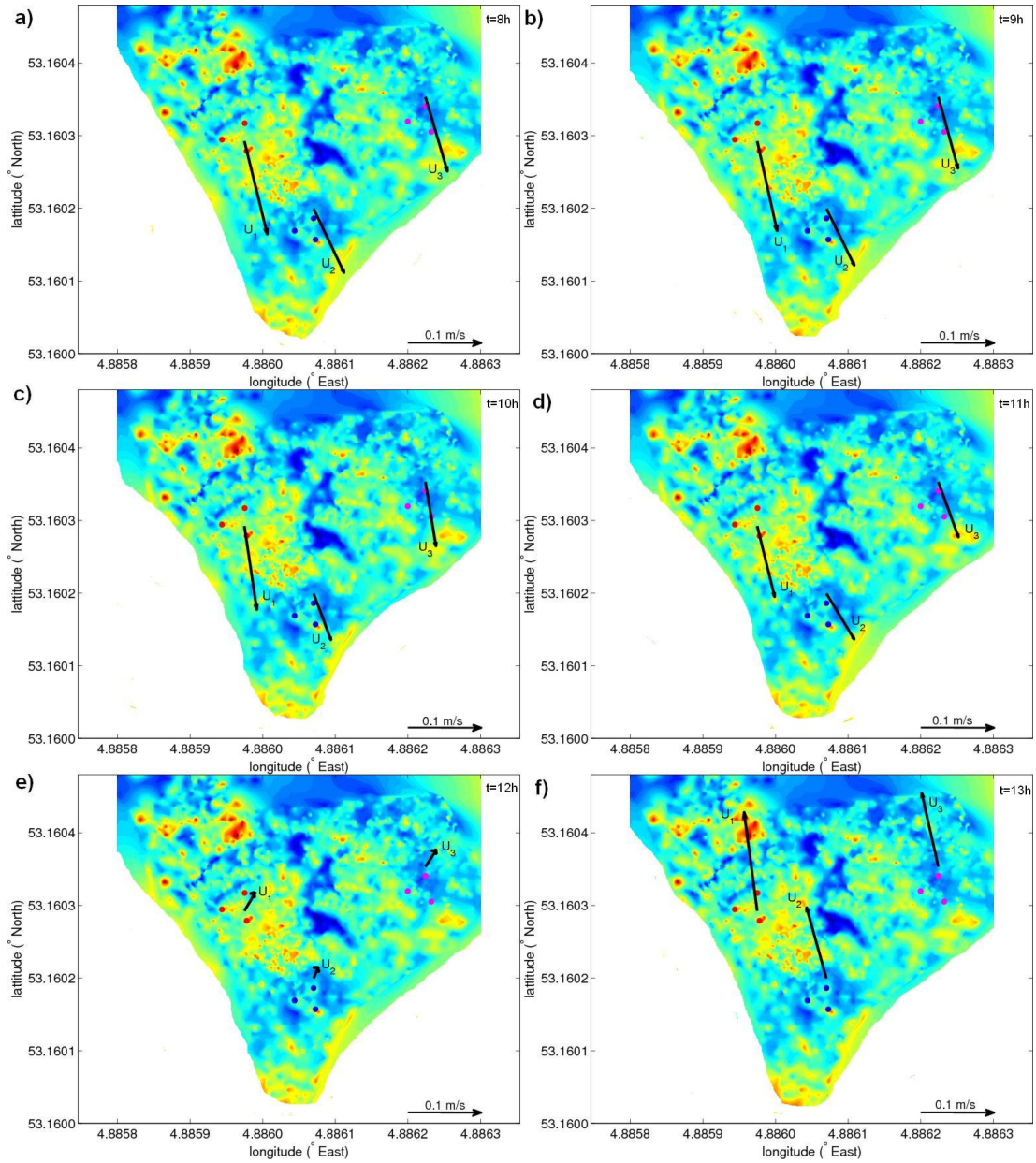


Figure 17: Overview of the magnitude and direction of the near bed currents on the measurement locations on and near the mussel patch with underlying bathymetry on 18/10. The vector arrows show the average current velocity U magnitude and direction of the previous 10 minutes at 6 moments during the tidal cycle. The subscript numbers indicate the measurement location and the colored dots indicate the positions of the measurement frame poles.

cation as on 01/10 that the flow lost more energy by traveling over the mussel patch than by traveling along the mussel patch. Again, this gives no indication for flow routing, since current velocities were significantly lower at frame 3 compared with frame 1 so that the flow decelerated also along the patch. Evidence for wake effects at the patch boundary might be found by plotting the w -current, which shows a w -current between -1.0 and -2.0 cm/s during ebb at frame 2. This increased w -current could be an indication that flow experienced some wake effects when flowing over the patch boundary onto the mussel patch. An overview of the current velocities on the measurement locations is shown in figure 17 at six periods during the tidal cycle.

4.3.3 Weak tide with high wind exposure from a southeastern direction

A relatively low peak in the current velocity in the first hour of the flood period was obtained on 24/10 with respect to the current velocity peaks on 01/10 and 18/10. The remainder of the tidal cycle shows that current velocities were relatively small during flood when the wind and current direction were opposing, while a following current and wind direction during ebb resulted in higher current velocities. The depth average current velocities did not show significant spatial differences during flood, but the current direction did as the current direction was directed more eastward at frame 2 with respect to frame 1 and even more eastward at frame 3. These differences are illustrated in figure 18g which shows vector arrows of the current velocity and direction over the tidal cycle. Mean flow direction during flood on 24/10 were 318° at frame 1, 310° at frame 2 and 299° at frame 3. This spatial difference around the mussel patch could indicate that the current refraction effects were obtained due to the oblique incidence of the current with respect to the mussel patch. Another effect might be the stimulation of flow routing along the mussel patch, because the current incidence angle forces a higher proportion of the flow around the patch. The effect of the incident current direction on the current velocities on and around the patch will be discussed in more detail in section 5.1. Highest shear velocities U_{*c} during flood were obtained at frame 1, while shear velocities were slightly lower at frame 2 and lowest at frame 3. An overview of the current velocities on the measurement locations is shown in figure 19 at six periods during the tidal cycle.

4.3.4 Vorticity

An oscillating pattern in the current velocities was recognized in the previous subsection on 18/10 (see figure 16) under the presence of a strong southwestern wind, while similar patterns were not clearly observed on 01/10 and 24/10 under different wind and tide conditions. This oscillating pattern was obtained at all measurement locations on and near the mussel patch. To investigate this phenomena a plot of the current velocity variations is shown in figure 20, where the current velocity variations were obtained by detrended current velocities from subtracting the 1 hour moving average from the current velocity. The variations were highest in the 1 hour period before slack tide as the amplitude of the variations showed a magnitude around 20% (about 2 cm/s). The observed variations appear to be periodic with a period of about 20 minutes and show up at all frames and computing of the cross-correlation

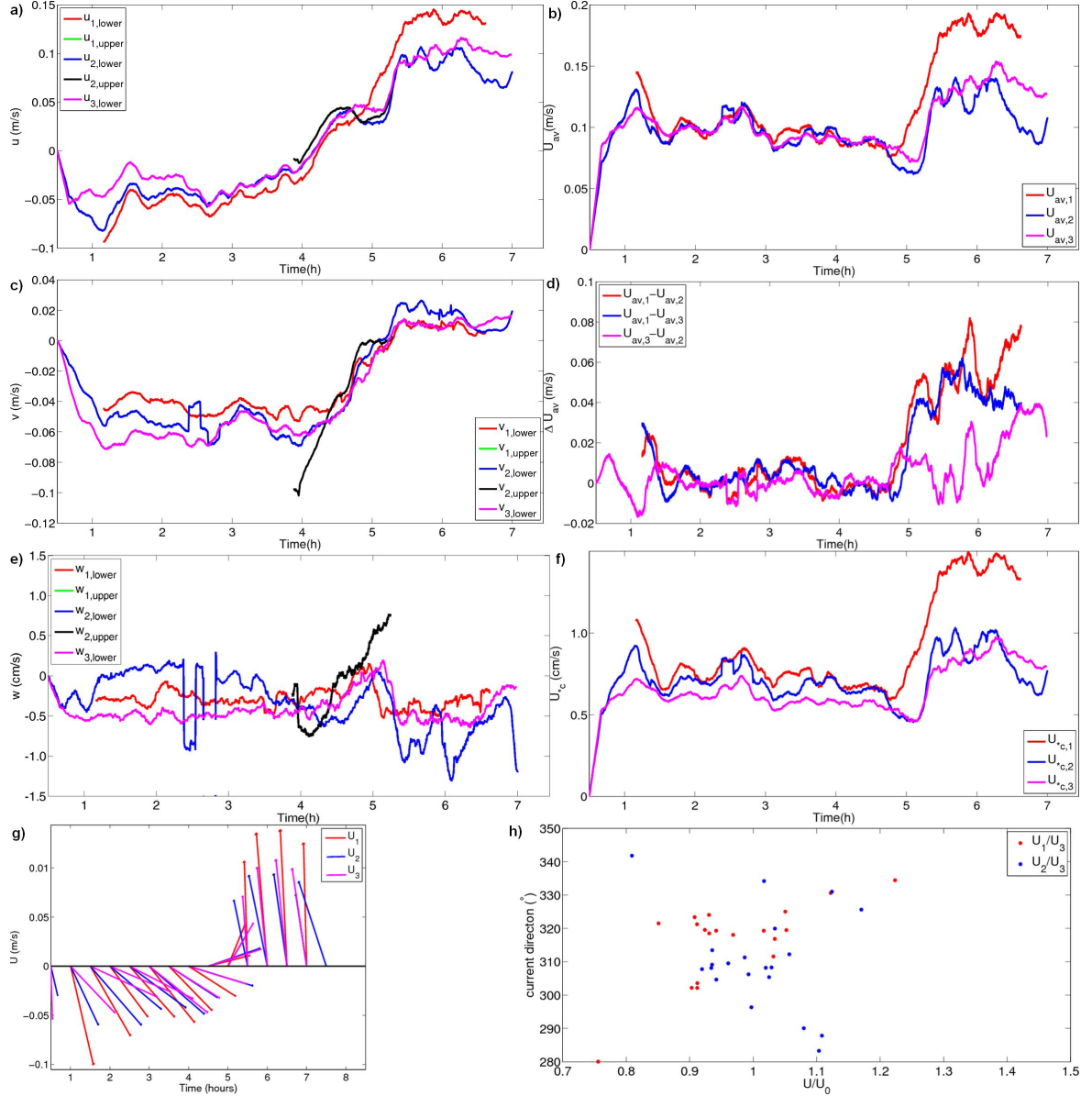


Figure 18: All panels show 10 minutes moving averaged values on 24/10 for all measurement locations. The subscripts denote the measurement location with numbers and the sensor position near the bed or away from the bed by lower and upper. *a)* Current velocity u ; *b)* Current velocity v ; *c)* Current velocity w ; *d)* Depth average current velocity; *e)* Difference of depth average current velocities between measurement locations; *f)* Current related shear velocity U_{*c} ; *g)* Current velocity vectors indicating the magnitude and direction of the flow (30 minute averages); *h)* Scaled current velocity as a function of the current direction. Current velocities at frames 1 and 2 are scaled by the free stream velocity U_3 .

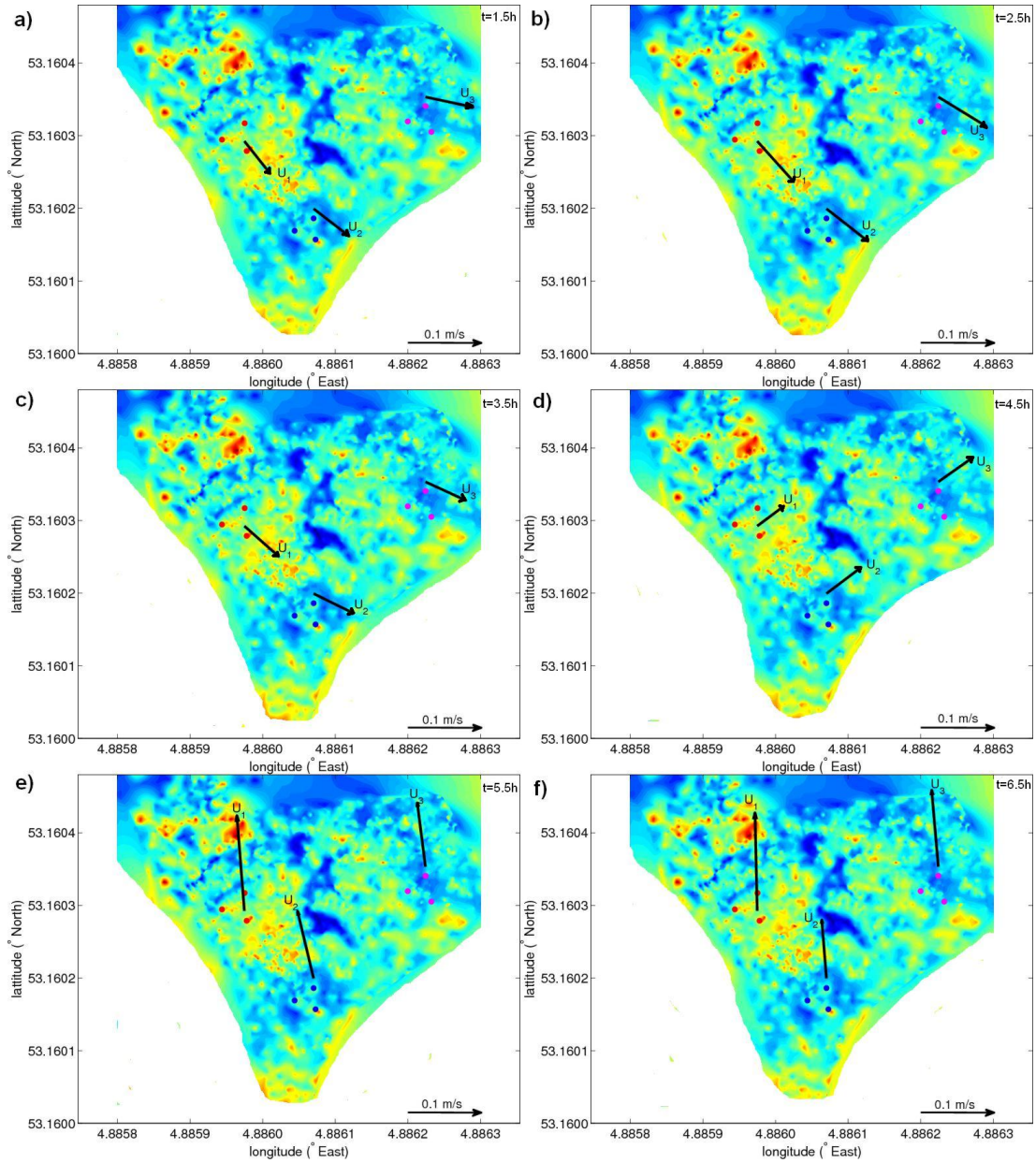


Figure 19: Overview of the magnitude and direction of the near bed currents on the measurement locations on and near the mussel patch with underlying bathymetry on 24/10. The vector arrows show the average current velocity U magnitude and direction of the previous 10 minutes at 6 moments during the tidal cycle. The subscript numbers indicate the measurement location and the colored dots indicate the positions of the measurement frame poles.

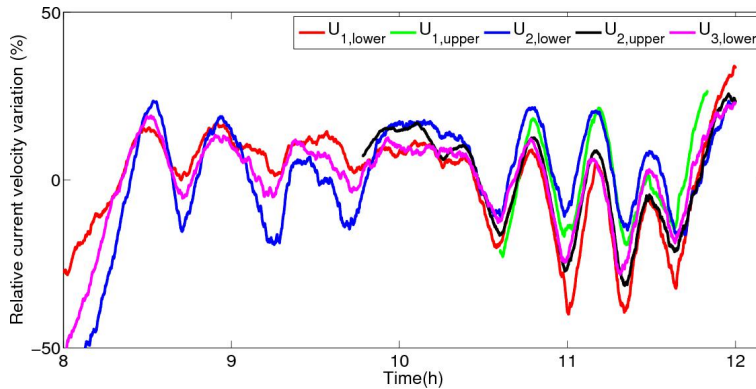


Figure 20: Relative variations of the current velocity with respect to the detrended current velocity $|U|$ (10 minutes moving average value - 1 hour moving average value) during flood on 18/10.

of the u - and v -currents showed that the oscillations of the u - and v -current were in phase. Using this period estimate, the length scale of this phenomena can be estimated as ~ 100 m. Comparing these results with literature shows similarities with Langmuir circulations, however variations in the vertical current w that are characteristic for Langmuir circulations were not obtained. Vorticity can also be generated by non-linear interaction of tidal oscillatory flow and topography [Robinson, 1981], where a small headland north of the mussel bed (see figure 6 might act as a topographic feature that is required for the vorticity generation. However these vorticity patterns cannot be related directly to the mussel patches yet, since it is unclear if these advected vortices are beneficial for mussel survival chances.

4.4 Waves

The wave height and mean wave direction were computed from velocimeter and pressure sensor data for each frame at each day. All relevant wave related parameters are plotted in figure 21, which shows the wave height, direction, spreading, peak period and near bed orbital velocity U_b in the three selected time series on 01/10, 18/10 and 24/10. These figures show that wave-current interaction plays an important role, because differences between the flood and ebb phase of the tidal cycle were obtained. Highest wave heights were obtained after slack tide during ebb and also variations in the wave directions were probably related to changes in the current directions. A similar pattern of relatively low near bed orbital velocities during flood and relatively high orbital velocities during ebb was obtained from the measurements. Measurements on 24/10 showed a different pattern since the orbital velocities were constant over the tidal cycle. The peak period of the waves was found to be relatively constant over the tidal cycle on 01/10, while a gradual decrease over time was obtained on 18/10 and 24/10. An overview of the averages over one tidal cycle of the wave related parameters from figure 21 is given in table 4.

The wave height and direction at the measurement site was compared with the

wave height and direction at offshore measurement station Eierlandse Gat to verify the relationship between offshore waves on the North Sea and the site (figure 9). The offshore wave direction at the North Sea did not correspond with the local wave direction during the measurement campaign, which confirms the statement in section 3.1 that waves were generated locally in the tidal channel eastwards of the site. However high wave heights were recorded at station Eierlandse Gat on 18/10 during a stormy period, coincide with slightly higher waves from northern to north-northwestern direction. This implicates that high waves propagated into the tidal inlet between Texel and Vlieland, where-after a portion of these incident waves propagated toward the measurement site due to refraction and thus causing a more northern incident wave direction at the measurement site.

Analysis of the spatial variations of the wave heights and directions was performed by plotting the dimensionless ratio H_{rms}/h over time and the root-mean-squared wave height as a function of the mean wave direction in a scatterplot for all conditions for all measurement locations on 01/10, 18/10 and 24/10 (figures 22 and 23). The compass plots show that the incident wave angle was relatively constant on day 32 and relatively variable on day 15. The average wave angle on day 32 was about 10 degrees, while the average wave angles on day 15 and day 38 were about 40 and 30 degrees respectively. An overview of the average wave directions per location is given in table 5. The scaled wave heights (figure 22) on 01/10 and 18/10 were relatively low in the first hours of the tidal cycle during flood and thereafter increased during ebb. The current and wave propagation direction was predominantly following during the flood current and opposing during the ebb current, while the wind direction and therefore the direction of wind related stresses was mainly opposing the wave propagation direction during flood and mainly following during ebb on 18/10. H_{rms}/h varied between 0.04 during flood and 0.10 during ebb on 01/10 and between 0.05 and 0.14 on 18/10. A different pattern of the scaled wave height over the tidal period was found on 24/10, where a relatively constant value of $H_{rms}/h = 0.09$ was found over the entire tidal cycle. The wind direction during this measurement interval on 24/10 was southeast, so the directions of wind related stresses and waves were predominantly perpendicular. The flood current and wave direction were also perpendicular, while the ebb current and wave direction were mainly opposing. Significant differences in the scaled wave heights between the measurement locations on the mussel patch and off the patch were not obtained from figure 22, probably due to the low incident wave heights and small patch size. The minimum condition for wave breaking ($H_{rms}/h > 0.3$) was never exceeded in the selected tidal periods, probably because potentially high incoming waves will already break on the higher elevated area between the mussel patch and the tidal channel (figure 10). Therefore it is not necessary to consider possible effects of wave breaking such as additional production of turbulent kinetic energy in further analysis of this study.

4.5 Turbulence

The turbulent kinetic energy (TKE), Reynolds shear stress and turbulence dissipation rate were computed to qualify the turbulence effects at the measurement frames. The velocity components of the near bed measurements were corrected for wave influence by using the correlation with the upper velocity measurements (0.5

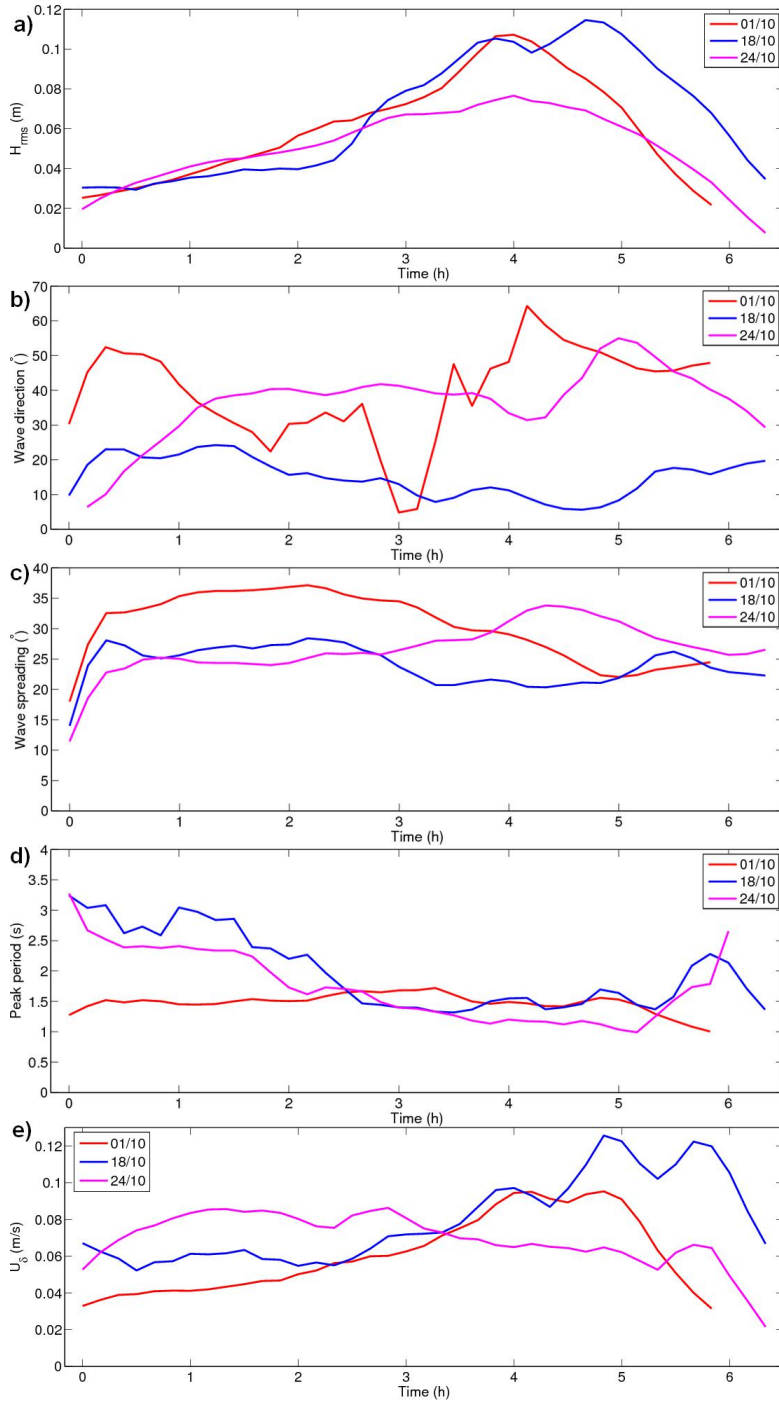


Figure 21: *a)* Root-mean-squared wave height H_{rms} , *b)* wave direction, *c)* wave spreading, *d)* peak frequency, *e)* peak orbital velocity. Colors indicate the various dates of the selected time series. X-axis shows the length of each tidal cycle in hours from the first detected signal at the pressure sensor, where the length of the tidal cycles varied due to different water levels. All data was obtained from the pressure sensor and velocimeter at frame 3.

Date	H_{rms} (m)	Dir ($^\circ$)	Spreading ($^\circ$)	T_p (s)	U_b (m/s)
01/10	0.06 ± 0.03	40 ± 13	30 ± 6	1.5 ± 0.2	0.06 ± 0.02
18/10	0.07 ± 0.03	15 ± 6	24 ± 3	2.0 ± 0.6	0.08 ± 0.02
24/10	0.05 ± 0.02	37 ± 10	27 ± 4	2.0 ± 1.4	0.07 ± 0.01

Table 4: Average values of wave related parameters H_{rms} , wave direction, wave spreading, peak period and near bed orbital velocity U_b during varying environmental conditions. All data was obtained from the pressure sensor and velocimeter at frame 3.

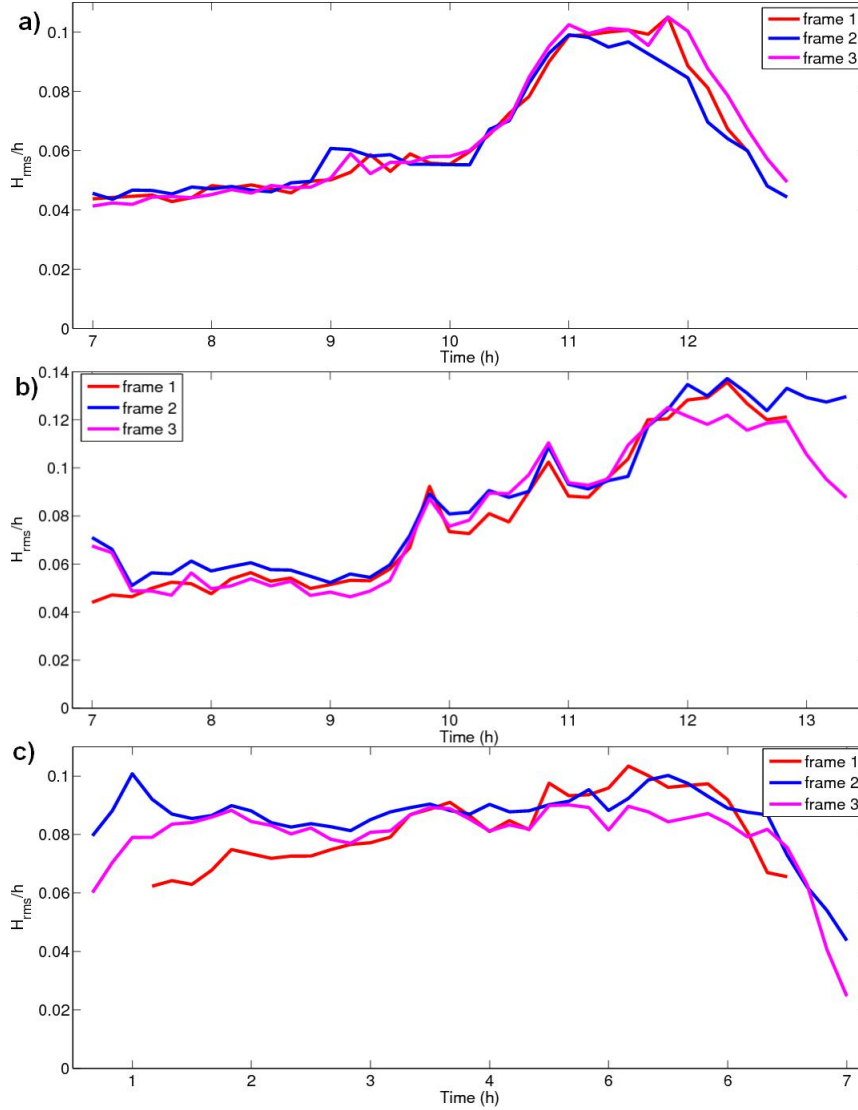


Figure 22: Scaled wave height H_{rms}/h as a function of time during one tidal cycle on all measurement locations on a) 01/10, b) 18/10 and c) 24/10.

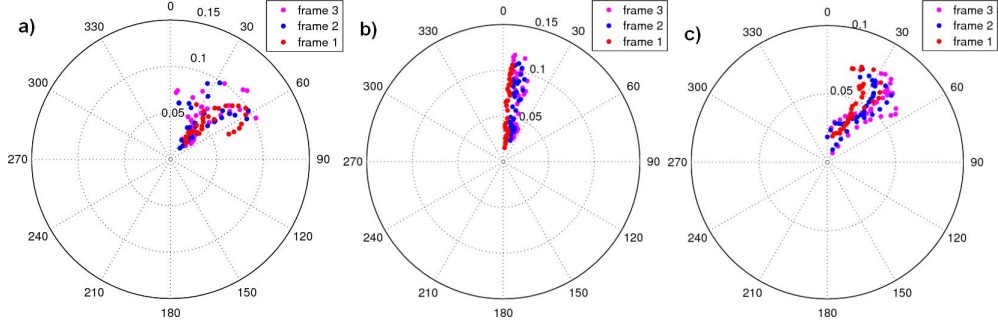


Figure 23: Compass plot of the mean wave directions in degrees as a function of the RMS wave height in meter (both 10 minutes average values) for all measurement locations. The wave direction 0 degrees corresponds with north, 90 degrees is east, 180 degrees is south and 270 degrees is west. Figure shows data of one tidal cycle on *a) 01/10, b) 18/10 and c) 24/10.*

Date	$H_{rms,1}$ (m)	$H_{rms,2}$ (m)	$H_{rms,3}$ (m)	Dir_1 ($^{\circ}$)	Dir_2 ($^{\circ}$)	Dir_3 ($^{\circ}$)
01/10	0.06 ± 0.02	0.05 ± 0.02	0.06 ± 0.03	45 ± 10	39 ± 12	40 ± 14
18/10	0.06 ± 0.03	0.06 ± 0.03	0.07 ± 0.03	5 ± 2	12 ± 4	15 ± 6
24/10	0.05 ± 0.02	0.05 ± 0.02	0.05 ± 0.02	25 ± 7	30 ± 10	37 ± 10

Table 5: Average values of wave height H_{rms} and wave direction during various environmental conditions on all measurement locations. The numbers in the subscripts indicate the measurement locations.

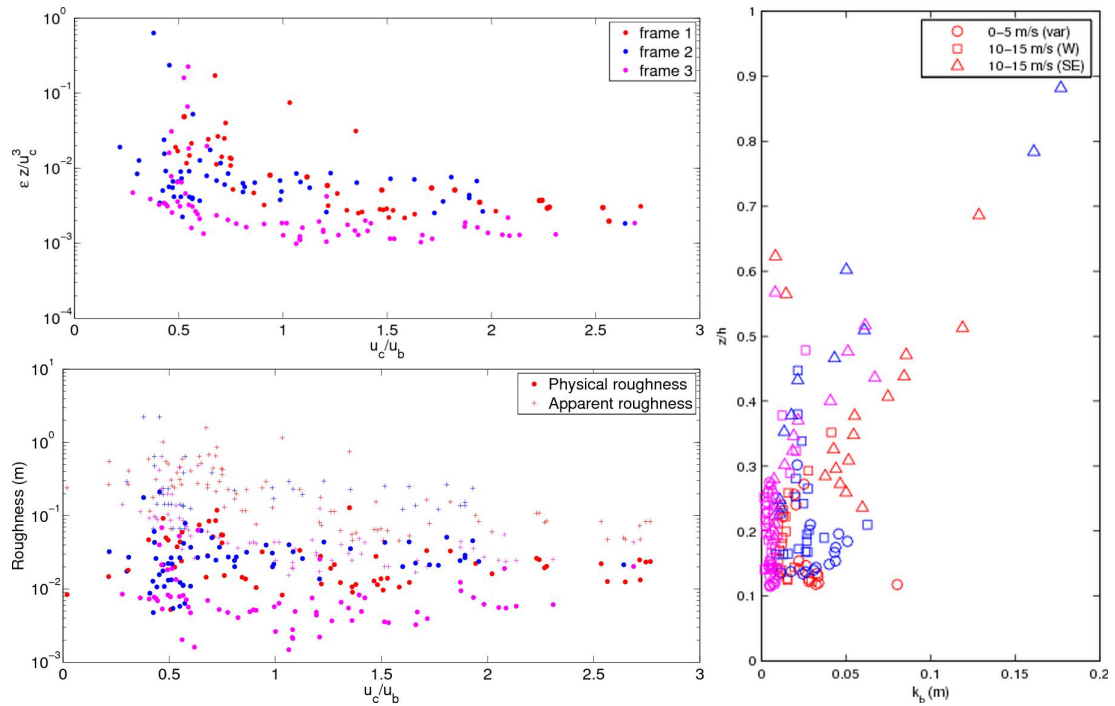


Figure 24: *a*) Dimensionless dissipation of TKE as a function of scaled current velocity (current velocity divided by wave orbital velocity). *b*) The apparent roughness height k_a , plotted with asterisks and physical roughness height k_b , plotted with dots. *c*) Physical roughness height k_b as a function of the relative water depth (height of ADV sensor above the bed divided by the total water depth) for 3 wind regimes (indicated with various marker symbols). All subfigures show measurements that were performed during flood on three selected days. Colors indicate the location of the measurements.

m above the lower ADV). However to correct the velocity components at frame 3 a different approach needs to be applied, because at this frame there are no upper velocity measurements. Therefore a pressure correction method was applied of which the results of this different correction method are discussed in the upcoming section.

4.5.1 Dissipation of TKE and roughness

Local estimates of the physical roughness height k_b were calculated for the selected data and for all frames. Estimating the surface roughness heights requires dissipation of TKE rates, which was calculated as described in section 2.1. Some problems occurred when applying the quality control checks as described in section 3.3, since the first quality control method that checks whether the frequency dependence of the u , v and w spectra equal $f^{-5/3}$ rejected all data in the selected periods. This problem probably arises because this quality control method was not developed for measurement close to a bottom with a high roughness length. Therefore this frequency dependence quality check was ignored and only the inertia quality check was

Wind speed	$k_{b,1}$	$k_{b,2}$	$k_{b,3}$
< 5 m/s (Var)	0.027 ± 0.005	0.033 ± 0.010	0.006 ± 0.002
10-15 m/s (W)	0.015 ± 0.006	0.024 ± 0.006	0.006 ± 0.005
10-15 m/s (SE)	0.059 ± 0.026	0.043 ± 0.048	0.018 ± 0.017

Table 6: Average estimated values of the physical roughness height on three location on and near the patch in three wind conditions. Subscript numbers indicate the location.

applied. The inertia related quality control method approved 27-36 % of the data at frame 1, 41-51 % of the data at frame 2 and 50-55 % of the data at frame 3. The scaled dissipation rate is plotted against the scaled current velocity (figure 24a), where the scaled current velocity is defined as the tidal current velocity divided by the wave orbital velocity. Here, z is defined as the height of the ADV sensor above the bed. The law of the wall (equation 8) predicts that dimensionless dissipation of TKE as a function of the scaled current velocity should be constant. However results show that the dimensionless dissipation of TKE decreased for increasing relative current velocities. Additional turbulence was created by waves, so that wave effects on the dissipation of TKE should be considered in the computation of the surface roughness heights. The apparent roughness height k_a and physical roughness height k_b are plotted in figure 24b as a function of the scaled current velocity u_c/u_b . This figure shows the effect of waves on the apparent roughness height, because the apparent roughness is high for relative low u_c/u_b values and decreases for an increasing scaled current velocity. This suggests that the apparent roughness is affected by turbulence that is generated in the wave boundary layer. In contrast to the apparent roughness height, there is no obvious relationship between between the u_c/u_b and the physical roughness height for most of the data. However, increased k_b -values can be obtained for a low u_c/u_b -ratio at frame 1. This varying dependency of k_b with respect to u_c/u_b is related to the local bathymetry/coverage due to flow recovering effects near the patch boundaries. Higher current velocities will extend the zone behind the patch in which the flow still experiences the mussel bed roughness, while it takes longer to produce a fully developed boundary layer after the upstream patch boundary on the mussel patch.

Because wind shear stress might generate additional turbulence and therefore might result in an overestimation of the dissipation rate of TKE [Jones and Monismith, 2008] and therefore also on the physical roughness height, these effects were analyzed by plotting the physical roughness height as a function of the relative water depth (figure 24c). The triangles on the right-hand side of the figure show that significant wind effects occur for the wind regime with high wind speeds from a southeastern direction, meanwhile high wind speeds from a western direction do not show a significant dependency to wind shear. This suggests that wind shear effects might be important if the wind direction is following the wave direction. An overview of the average physical roughness heights for each location and wind condition is given in table 6 and shows an overestimation of the k_b -values for the third wind condition.

The effects of the wind and waves on the measurements of turbulent kinetic en-

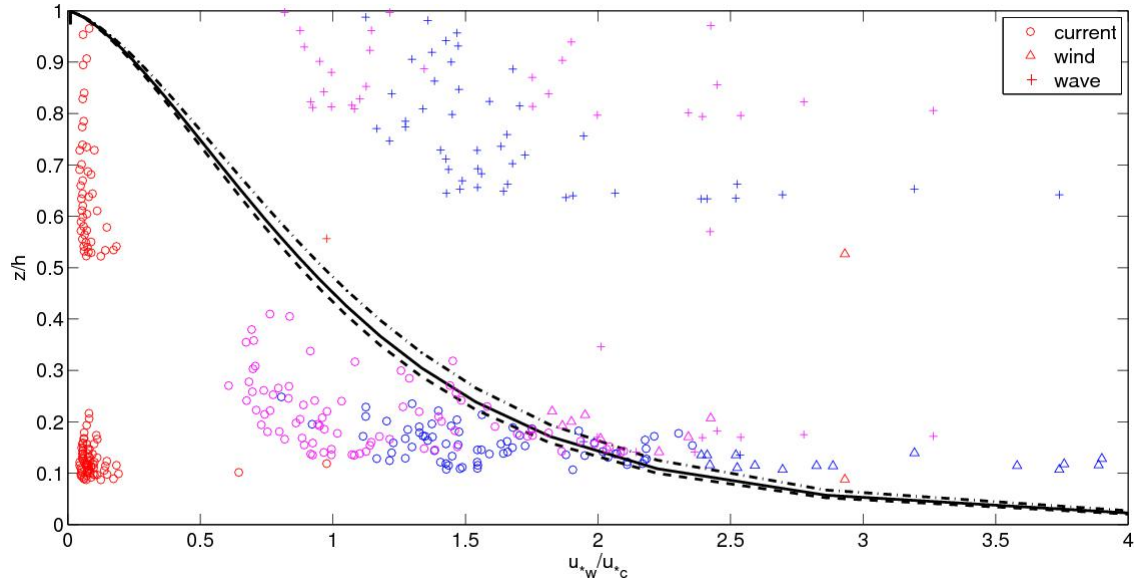


Figure 25: Relative water depth (height of ADV sensor z above the bed divided by the total water depth h) versus the ratio between the current related and wind stress u_{*w}/u_{*c} . Dissipation measurements of ϵ were classified according to the most appropriate scaling: wave affected surface layer (equation 21, crosses), wind stress log-layer (equation 22, triangles) and current related bed shear stress log-layer (equation 5, circles). Theoretical transition depths between the current related bed stress log-layer z_{t3} (equation 25) are plotted for maximum observed wave heights on 01/10, 18/10 and 24/10 by respectively black dash-dotted, dashed and continuous lines for conditions experienced on these days. The colors indicate the measurement series on 01/10 (red), 18/10 (blue) and 24/10 (magenta).

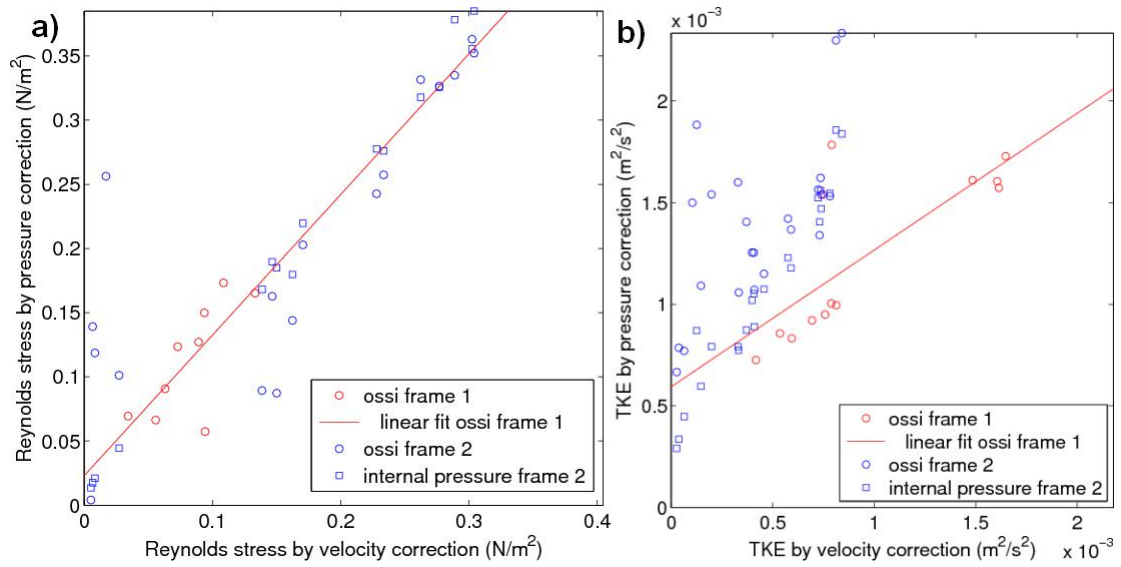


Figure 26: *a)* Reynolds stress by current velocity sensor correction versus Reynolds stress by pressure sensor correction at frame 1 and 2. *b)* TKE by current velocity sensor correction versus Reynolds stress by pressure correction at frame 1 and 2. Circles indicate correction by the ossi pressure sensor at the measurement frame, squares indicate correction by the internal ADV pressure sensor and the solid line represents the linear best fit through the ossi corrected data points at frame 1.

ergy dissipation were classified by comparing the measurement heights above the bed of the ADV sensors with the transition heights between the layers, z_{t2} and z_{t3} (see figure 3). The results are plotted in figure 25 together with the theoretical transition heights z_{t3} and show that most of the measurements that were classified as scaling due to current related bed stress are below the theoretical transition height, while the wind stress related measurements are above the theoretical transition height. Therefore this classification of measurements by comparing to the transition heights between the layers as described by Jones and Monismith [2008] seems to give appropriate results. The current related bed shear log-layer dominated the entire water column due to low wind shear stresses and high tidal currents on 01/10, while the effects of wind and waves were clearly present on 18/10 and 24/10. The dissipation rates in the upper part of the water column were dominated by the waves on 18/10 and 24/10, while a wind stress log-layer developed close to the bed above a ratio of $u_{*w}/u_{*c} = 1.8$ and almost the entire water column was dominated by wind stresses or waves. Note that few measurements were present in the middle part of the water column due to the experimental setup of the upper and lower ADV sensors.

4.5.2 Reynolds stress and turbulent kinetic energy

Alternative methods to determine the Reynolds stress and TKE were tested by plotting the Reynolds stress and TKE that were computed using the upper velocity

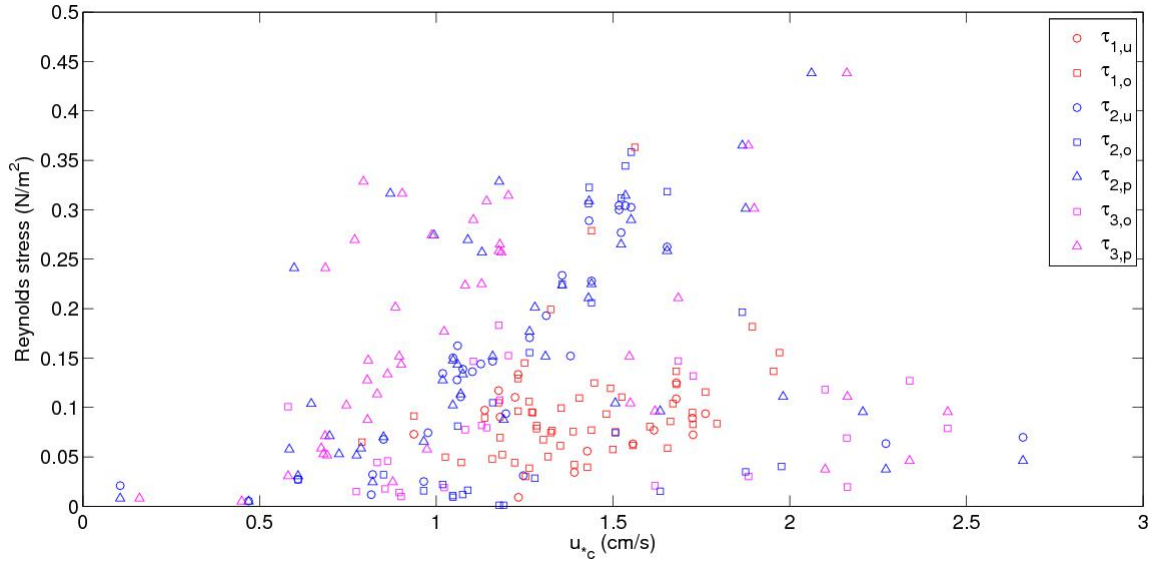


Figure 27: Reynolds stress as a function of current related bed shear velocity U_{*c} of all measurement locations. The symbols indicate the correction method that was used: circles, squares and triangles for respectively using the upper ADV sensor u , ossi pressure sensor o and internal ADV pressure sensor p as a correction signal.

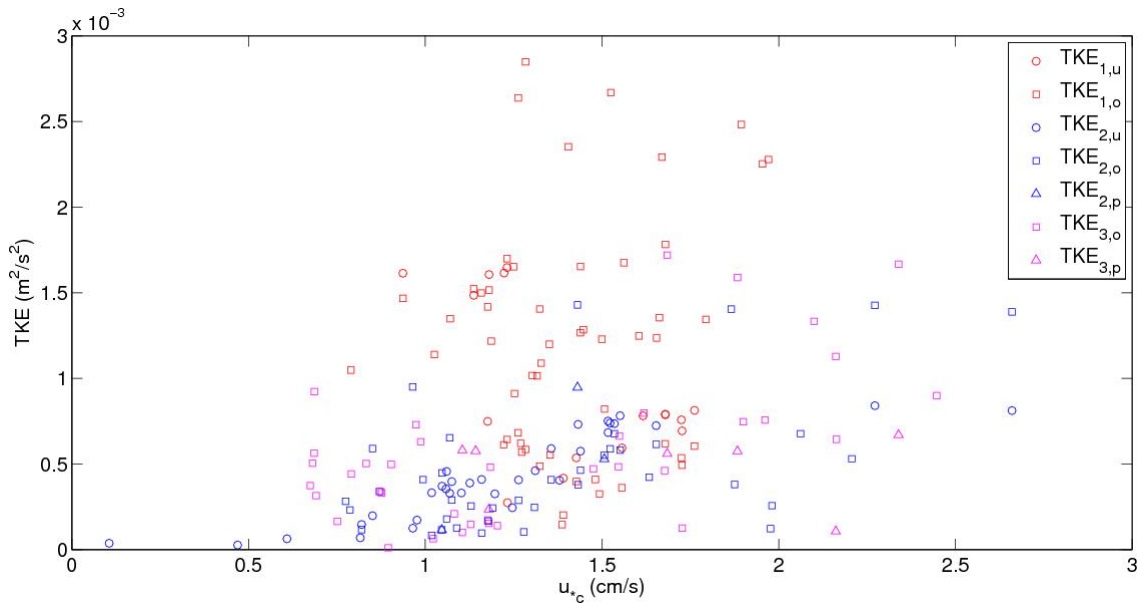


Figure 28: TKE as a function of the current related bed shear velocity U_{*c} of all measurement locations. The symbols indicate the correction method that was used: circles, squares and triangles for respectively using the upper ADV sensor u , ossi pressure sensor o and internal ADV pressure sensor p as a correction signal.

	a	b	R^2	N
$\tau_{o,1}(N/m^2)$	1.1	0.023	0.48	53
$\tau_{o,2}(N/m^2)$	0.79	0.08	0.91	40
$\tau_{p,2}(N/m^2)$	1.2	0.0077	0.82	38
$TKE_{o,1}(m^2/s^2)$	0.67	$5.9 \cdot 10^{-4}$	$2.32 \cdot 10^{-5}$	53
$TKE_{o,2}(m^2/s^2)$	0.95	$9.8 \cdot 10^{-4}$	$1.0 \cdot 10^{-3}$	40
$TKE_{p,2}(m^2/s^2)$	1.6	$3.4 \cdot 10^{-4}$	$4.0 \cdot 10^{-5}$	38

Table 7: Slope a , intercept b , total error R^2 and number of measurement points N of the ossi and internal ADV pressure correction methods with respect to the upper velocimeter correction method for frames 1 and 2 and for the Reynolds stress and TKE (plotted in figure 26).

ADV sensor method versus the Reynolds stress and TKE that were computed using respectively the ossi pressure sensor and internal ADV pressure sensor signals. Then the relationship between the velocity and pressure corrected Reynolds stress and TKE can be determined by computing linear best fits ($y = ax + b$), which are shown in figure 26 in case of the ossi pressure corrected Reynolds stress and TKE at frame 1. The results of this linear regression method (table 7) indicate that overall the pressure correction methods gave a reasonable good performance and can be used to estimate the Reynolds stress and TKE in addition to the upper ADV velocity correction method, although a higher error R^2 was obtained for the ossi corrected TKE at frame 2. Note that internal pressure correction at frame 1 is ignored, because of unreliable measurements of this internal pressure sensor.

The turbulent kinetic energy and Reynolds shear stress as defined in equations 2 and 3 were computed as described in section 3.3. The Reynolds stress and TKE of the selected measurement periods (01/10, 18/10 and 24/10) are shown in figures 27 and 28. Only measurements that were categorized in the current boundary layer, as determined in the previous subsection, were plotted in these figures. Figure 27 shows that the observed Reynolds stresses tend to increase as a function of the shear velocity U_{*c} , but the sensitivity of the Reynolds stress with respect to the shear velocity appears to be stronger at frame 2 than at frame 1. Generally higher Reynolds stresses were obtained at frames 2 and 3 compared with frame 1. These measured Reynolds stresses together with an approximation of the vertical velocity gradient as $\partial u/\partial z \approx \Delta u/\Delta z$, where Δu and Δz are respectively the differences between the current velocities and elevation above the bed between the upper and lower ADV sensors, can be used to estimate the eddy viscosities on the patch and downstream of the patch. These eddy viscosities characterize the vertical mixing in the water column, which is important for the mussels because the vertical mixing provides a vertical supply of food to the mussels. Then using equation 3 yield estimates of $\mu_{t,1} = 5 \cdot 10^{-2}(Pa \cdot s)$ and $\mu_{t,2} = 1.5 \cdot 10^{-2}(Pa \cdot s)$, so the transfer of momentum due to turbulent eddies and therefore the vertical mixing is higher above the patch than downstream of the patch. Note that it was not possible to make an estimate of μ_t further away of the patch, because of the single ADV sensor at frame 3. Meanwhile higher TKE values, which also increase as a function of the shear velocity U_{*c} , were

obtained at frame 1 with respect to frames 2 and 3. These higher TKE values indicate that the upstream patch boundary generates more TKE that was advected to frame 1 than the downstream patch boundary.

4.5.3 Bed shear stress

The previous section described how the interaction between wind, waves and currents affects the water column and therefore it is important to analyze the interaction between a wind induced surface shear stress, wave related to determine the total bed shear stresses. The current and maximum wave related bed shear stresses were calculated using equations 10 and 16. Then current-wave interaction effects were calculated using equation 18. The time series of the bed shear stress τ_b in figure 29 shows that the total bed shear stress τ_{cw} was slightly higher than the wave related bed shear stress τ_w , while the current related bed shear stress τ_c generally was much lower than τ_{cw} and τ_w . Relatively high current related bed shear stresses with respect to the total bed shear stresses were found early in the flood period (figures 29b,c) and current related bed shear stresses gave a significant contribution to the total shear stress during low wind speeds at 01/10 (figure 29a). The various environmental conditions resulted in different relationships of the bed shear stress during the flood period. Figure 29a shows maximum total bed shear stresses about an hour before slack tide, while figures 29b and 29c show maximum bed shear stresses towards the end of the flood period and early in the flood period respectively. This suggests that the interaction of the wind, wave and current related shear stresses plays a significant role with respect to the total experienced bed shear stress on each measurement location.

Analysis of the differences in total bed shear stress between the measurement locations shows that bed shear stresses off the mussel patch at frame 3 were generally lower than on or near the patch at frames 1 and 2. Maximum total bed shear stresses τ_{cw} of $1.1 N/m^2$, $1.2 N/m^2$ and $0.6 N/m^2$ were obtained at frames 1, 2 and 3 at 01/10 (figure 29a), where current related bed shear stresses τ_c contributed up to 40 % of the total bed shear stress for frame 1. Despite of the lower current related bed shear stress, the total bed shear stress behind the patch boundary at frame 2 is slightly higher than on the patch at frame 1 due to the higher contribution of wave related shear stress. This difference in total bed shear stress between frames 1 and 2 is significantly larger at 18/10 (figure 29b) due to the higher contribution of the wave related bed shear stress. This higher wave related bed shear stress can be associated with the difference in wave direction between 18/10 and 01/10 (figure 23), which shows that waves propagated mainly over the mussel patch at 18/10 and mainly alongside of the patch at 01/10. Therefore waves experienced a higher friction factor at 18/10 and thus a higher wave related and total bed shear stress. On the other hand the contributions of the current related bed shear stresses to the total shear stresses were relatively small at 18/10 compared with 01/10 with a maximum current related contribution of 20% of the total bed shear stress on the patch (frame 1). Different environmental conditions on 24/10 (figure 29c) resulted in higher total bed shear stresses on the patch (frame 1) and far off the patch (frame 3) with respect to the conditions on 01/10 and 18/10.

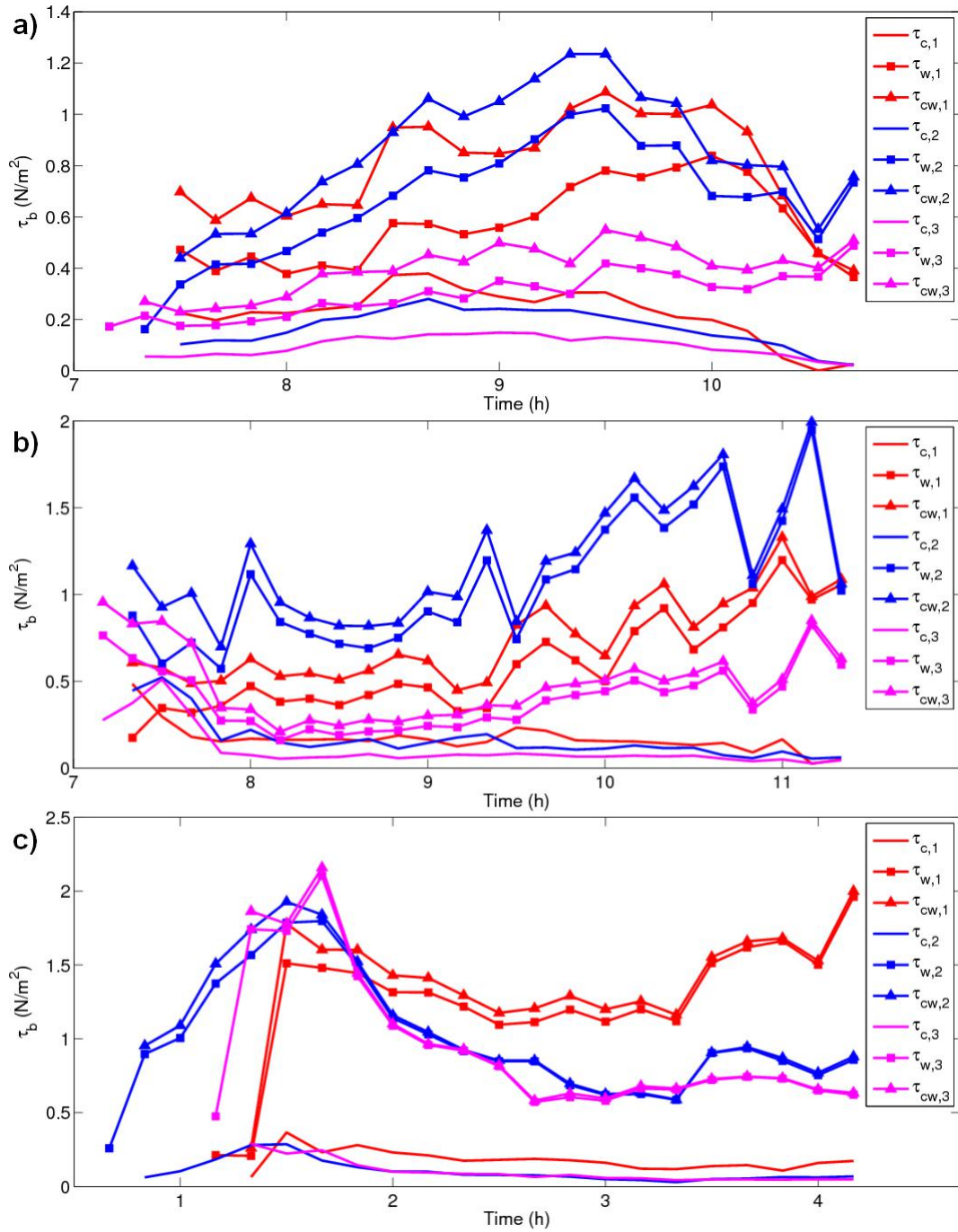


Figure 29: Current related (τ_c), wave related (τ_w) and wave-current interaction bed shear stress (τ_{cw}) as function of time during flood. Colors indicate the measurement locations. a) 01/10 b) 18/10. c) 24/10.

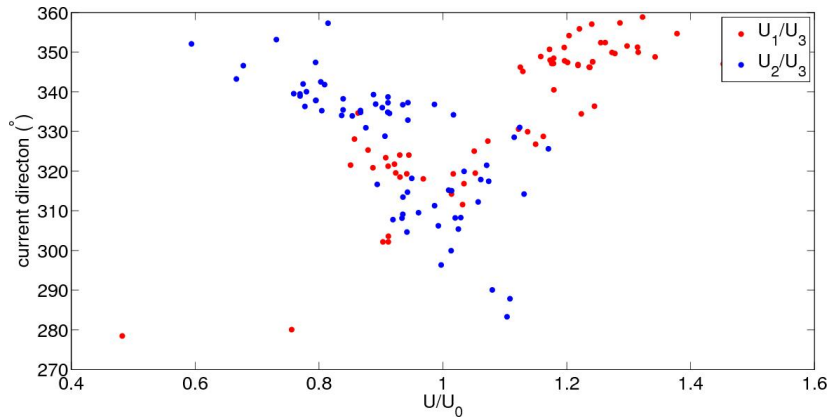


Figure 30: Current velocities at frames 1 and 2 scaled by free stream velocity U_3 as a function of the current direction.

5 Discussion

5.1 Effects of a mussel patch on hydrodynamics

Current velocity measurements on and near a mussel patch were obtained to study the current velocity patterns on and around this mussel patch. These measurements showed that current velocities appeared to accelerate when entering the mussel patch, because higher depth average velocities were obtained on the patch near the patch boundary (frame 1) with respect to the relatively undisturbed flow further away of the patch (frame 3). Meanwhile current velocities appeared to decelerate behind the mussel patch as depth average current velocities were found to be lower downstream of the patch boundary (frame 2) with respect to the relatively undisturbed flow further away of the patch. These higher current velocities on the patch near the upstream boundary could be explained by the overshooting phenomena as proposed by Folkard and Gascoigne [2009] which means that the flow decelerates close to the bed due to the suddenly increased bed friction due to the mussel roughness and increases in the rest of the water column above the current boundary layer. However velocity differences between the upper and lower part of the water column were obtained behind the downstream patch boundary at frame 2 rather than on the patch at the upstream patch boundary (figures 14a and 16b). This imbalance behind the patch implies that the flow is still in a readjustment zone at approximately 1 m behind the patch boundary and experiences the mussel bed roughness, while the velocity balance on the patch suggests a vertically mixed water column. However higher current velocities on the patch near the patch boundary could also be obtained when flow routing effects developed, since figure 4 showed that a diverging flow could be obtained near the patch boundary. Additionally a relationship between the current direction and relative current magnitude was found (shown in figure 30), because currents directed from the north-northwest resulted in higher current velocities on the patch with respect to the current velocities downstream of the patch than current directed from the northwest and vice versa. This indicates that possibly flow routing effects were present, as flow from a northwestern direction forced the current along the mussel patch while a flow from a north-northwestern

direction forced the current over the mussel patch. However figure 10a shows that some features, which represent small oyster patches, were present upstream of the patch boundary and therefore affect the flow towards the mussel patch as well. Also the current velocity directions behind the patch and further away of the patch (figure 14g -18g) were generally directed more towards the east compared with the velocity directions that were observed on the patch at frame 1, so their v -components were higher. These differences in the current flow direction might be induced due to flow routing around the patch as well, but also current refraction and reflection effects might play a role.

Analysis of the wave heights around the mussel patch showed that there were no significant differences between the measurement locations, because incoming waves did not propagate in the same direction over the mussel patch from frame 1 towards frame 2 like the flood current. Also incoming waves lost most energy before arriving at the mussel patch due to the dominant north-northeastern to northeastern direction of the waves, which can be nearly perpendicular to the current direction, which causes waves to propagate over a shallow area before reaching the investigated mussel patch (figure 10b). However even small waves were still important for wave-current interactions and determining the total bed shear stresses. This is illustrated by figure 29 which shows that wave related bed shear stresses were usually much higher than current related bed shear stresses and therefore the total bed shear stresses were dominated by the wave related bed shear stresses. The various environmental conditions resulted in different relationships of the bed shear stresses during the flood period, which underlines that interaction between wind generated surface shear stresses, wave generated shear stresses and current related bed shear stresses affects the total bed shear stresses. These wave dominated total bed shear stresses τ_b around 1-2 N/m^2 agree with Donker et al. [2012].

Hydrodynamics on the mussel patch showed a sensitivity to the environmental conditions because the wind speed and direction and the tidal range affected the current velocity magnitude and direction and wave direction. The differences in hydrodynamics on the patch were shown in figures 11-13, 21 and 23 and finally the combined effects of wave-current interaction on the bed shear stress τ_b were shown in figure 29. The interaction between wind stress and currents and waves was found to be an important, because the wave and current directions were influenced by the wind stresses. Therefore flow patterns changed and were more forced to flow over the patch or routed around the patch. Subsequently higher wind stresses resulted in increased turbulent mixing, because the transition depth between the current related bed stress log-layer and the wind stress log-layer and wave affected surface layer scaled as a function of the current related bed shear stress and wind surface stress U_{*w}/U_{*c} (figure 25).

5.2 Effects of a mussel patch on turbulent mixing

The turbulent dissipation rate ϵ showed a dependency to the scaled current velocity U_c/U_b as the dissipation of TKE increased for high wave orbital velocities U_b with respect to the current velocity U_c , however the dissipation of TKE became constant for relatively high current velocities with respect to the wave orbital velocities (fig-

ure 24a). The measured dissipation of TKE was higher on the patch and close to the patch with respect to free stream measurements. A comparison of the TKE dissipation rates on the upstream and downstream patch boundaries showed that $\epsilon z/U_c^3$ was relatively high on the upstream patch boundary for low current velocities since higher turbulent dissipation rates were found on the patch than behind the patch. On the other hand high current velocities resulted in higher TKE dissipation rates behind the patch with respect to measured values on the patch. This can be explained by the fact that it will take longer to produce a fully developed boundary layer after the upstream patch boundary for higher current velocities, while a turbulent eddy viscosity is advected further downstream of the patch.

Roughness lengths that were calculated using ϵ showed much larger values on a flat bottom than measured by Van Duren et al. [2006] (table 1). However Van Duren et al. [2006] found higher z_0 values above mussels than were obtained in this research. A current of 0.13 m/s corresponds with a $k_b = 0.156$ m according to Van Duren et al. [2006], while Folkard and Gascoigne [2009] obtained k_b values between 0.03 and 0.09 m for a free stream velocity of 18.4 cm/s and Van Leeuwen et al. [2010] proposed a k_b value of 0.03 m independent of the free stream velocity. During very low wind exposure the ϵ based calculation resulted in k_b -values of respectively 0.027 ± 0.005 and 0.033 ± 0.010 near the upstream patch boundary (frame 1) and behind the downstream patch boundary (frame 2), while $k_b = 0.006 \pm 0.002$ on a flat bottom (frame 3) (table 6). Donker et al. [2012] found slightly higher roughness lengths around $k_b = 0.05$ in the same area. Differences between the roughness length as obtained in this study and by Donker et al. [2012] may be related to the stricter use of the quality control methods on the calculation of TKE dissipation rates. The roughness length in the relatively uncovered area closely behind the mussel patch (frame 2), is largely underestimated when using a flat bottom approximation from Van Duren et al. [2006]. The uncovered flat bottom roughness length (frame 3) is largely underestimated as well. Therefore classifications between a mussel covered bed and a flat bottom from flume experiments are insufficient for field experiments. Probably advection of turbulent eddy viscosity has an important role for interpreting higher z_0 values at frames 2 and 3. A comparison between the measurement locations showed that k_b values were relatively large at the mussel patch and behind the mussel patch with respect to the free stream uncovered area away of the mussel patch. In general the patch boundary resulted in higher k_b values behind the patch-gap boundary than on the mussel patch itself, so that the patch boundary enhanced the turbulent dissipation rate.

Categorizing of the ϵ -values using Jones and Monismith [2008] showed that even close to the bed ($z/h \approx 0.2$) ϵ scaled according to the wind stress log-layer in case of high wind velocities ($U_{*w}/U_{*c} > 1.7$). The classification of the measured ϵ -values agreed quite well with the theoretical transition height of the current related bed shear log-layer (figure 25). Nevertheless the estimates of the physical roughness height showed variations for different environmental conditions, which is in contradiction with Donker et al. [2012]. This implies that the variations in the current direction and magnitude due to the interactions of the wind stress and waves result in variations in the observed ϵ -values and therefore also to variations in the k_b -values. Another possibility is that the methods that were used to remove effects of the wind and wave related ϵ -values were insufficient.

The observed Reynolds stresses were found to increase as a function of the current related shear velocity, while relatively high Reynolds stresses were obtained behind the downstream patch boundary and relatively low Reynolds stresses on the patch near the upstream patch boundary. The results of the measured Reynolds stresses can be compared with the flume study results that were found by the single patch experiments of Folkard and Gascoigne [2009]. The depth-average current velocities above and behind the mussel patch at frames 1 and 2 between $t = 8h$ and $t = 10h$ on 01/10 are close to the free stream velocity of 0.184 m/s that was used by Folkard and Gascoigne [2009]. Measurements showed Reynolds stresses around $0.3 N/m^2$ behind the patch at frame 2, $0.1 N/m^2$ above the patch at frame 1 and around $0.15 N/m^2$ at the uncovered area at frame 3. Folkard and Gascoigne [2009] obtained maximum Reynolds stresses around $0.05 N/m^2$ before the patch, $0.3 N/m^2$ above the patch and about $0.1 N/m^2$ at 1 meter behind the patch. So the order of magnitude is equal, but field measurements show a higher Reynolds stress behind the patch than onto the patch just behind the smooth-rough boundary. Also the uncovered area measurements at frame 3 suggest higher flat bottom Reynolds stresses than assumed by Folkard and Gascoigne [2009]. Therefore this relatively high τ_{uv} behind the patch-gap boundary at frame 2 on 01/10 indicates that the passage of the flow over the mussel patch boundary off the mussel patch enhances the turbulence generation, while the passage over the patch boundary onto the mussel patch before frame 1 is less important for the turbulence generation. Because free stream velocities of 4 and 8 cm/s as used by Lassen et al. [2006] are smaller than the observed current velocities on the patch and downstream of the patch, smaller maximum Reynolds stresses of $0.05 N/m^2$ at 8 cm/s cannot be related to the results of this study. Lassen et al. [2006] showed that Reynolds stresses are high in the boundary layer and the height above the bed at which the maximum Reynolds stress occurs depends on the stream velocity. The deviation of the obtained Reynolds stresses from the maximum Reynolds stresses are unknown, because they were calculated at one height close to the bed in this study. So Reynolds stresses in this study were probably underestimated with respect to Folkard and Gascoigne [2009], because the measurement setup did not allow determination of the height above the bed at which the maximum Reynolds stress occurs.

TKE values increased as a function of the current related shear velocity, similar to observed Reynolds stresses. TKE values around $0.15 (cm^2/s^2)$ and around $0.05 (cm^2/s^2)$ were obtained respectively on the patch near the upstream patch boundary (frame 1) and both downstream of the patch and away from the patch (frames 2 and 3). Folkard and Gascoigne [2009] found depth-average TKE values of $0.1 (cm^2/s^2)$ before the patch and $0.2 (cm^2/s^2)$ above the patch and behind the patch for a free stream velocity of 0.184 cm/s, while the maximum TKE values around $0.25 (cm^2/s^2)$ were obtained at the rough to smooth patch boundary. Lassen et al. [2006] obtained maximum TKE values of $2.5 (cm^2/s^2)$ at a height of 4 cm above the bed for a free stream velocity of 8 cm/s, while TKE values of $0.5 (cm^2/s^2)$ were found above an uncovered bed. So the TKE values in this field experiment are comparable with Folkard and Gascoigne [2009], but smaller than those found by Lassen et al. [2006]. However these differences between this study and Lassen et al. [2006] are probably caused by the different measurement heights above the bed, because the TKE is concentrated near the bed. Especially because Folkard and Gascoigne [2009]

found that TKE is more concentrated near the bed downstream of a patch boundary.

5.3 Implications of patchiness for mussel beds

Estimates of the eddy viscosity and TKE indicated that the upstream patch boundary increased turbulence levels, which enhanced the vertical mixing in the water column and is therefore beneficial for mussels. This supports the assumptions by Folkard and Gascoigne [2009] and Van de Koppel et al. [2005] that the presence of patch boundaries and gaps between patches enables the vertical food supply. Strong flow routing effects would have a negative impact on the mussels that are further away of the upstream patch boundary, since the a decrease of the current velocity means a decrease of the food supply. However flow routing could be beneficial for mussels at the edges of the patch, because of enhanced turbulent mixing due to shear-layer vortices (as in figure 4). These effects might explain why patch sizes are limited and explain observations of poor growth rates and die-off of mussels near the center of a mussel patch ([Okamura, 1986] and [Folkard and Gascoigne, 2009]). However these assumptions cannot be established with the results of this research.

5.4 Removing wave bias with pressure sensors

An approved method of removing wave bias from a current velocity time series using the correlation with a second current velocity time series ([Trowbridge, 1998]; [Feddersen and Williams, 2007]) to compute the Reynolds stress and TKE was extended by using ossi and internal ADV pressure time series as alternative correlation time series. Advantages of this extended method is that longer Reynolds stress and TKE time series can be computed, since the duration of the upper velocity time series is limited due to its low submersion time. Furthermore information of the Reynolds stress and TKE away of the patch at frame 3 can be gained, since only a single ADV sensor was available at this measurement location. These alternative methods to determine the Reynolds stress and TKE gave useful estimates in addition to the upper velocity correction method, because the pressure corrected Reynolds stresses and TKE could be considered as a linear function of the original velocity corrected Reynolds stresses and TKE. Only the ossi corrected TKE estimate at frame 2 was less accurate, whereas the estimates with the internal ADV pressure sensor at frame 1 showed no correlation at all.

6 Conclusions

The hydrodynamics over a mussel patch were obtained to investigate the effects of organization of mussels in a patch structure. Therefore current velocities and turbulence parameters were obtained at three locations on the patch near the upstream boundary, behind the downstream patch boundary and further away of the patch. Higher current velocities on the patch near the upstream patch boundary with respect to current velocities behind the downstream patch boundary and beside the patch were obtained under typical environmental conditions. These current velocity measurements showed weak indications for flow routing, because current velocity magnitudes were affected by the current direction. Also lower current velocities behind the downstream patch boundary might indicate flow routing around the mussel patch if measurements at this position were obtained in the wake zone of the mussel patch. However the setup of the measurement equipment was insufficient to obtain a conclusive proof. The measurements of TKE indicate that vertical mixing was enhanced when flow passes the patch boundary. Increased vertical mixing is advantageous for mussels because it increases the food supply and makes a patch boundary profitable for mussel survival chances. However, higher bed roughness values and a relatively high velocity gradient $\Delta u/\Delta z$ were obtained behind the downstream patch boundary. This implies that the flow was still in recovery of the patch boundary at the measurement locations behind the patch and experiences the roughness of the mussel bed, while roughness values at the measurement locations on the patch can be relatively low because the boundary layer need a certain time to become fully developed. Effects of the patch roughness with respect to the wave height were not obtained, because of the orientation of the measurement equipment with respect to the main wave direction and because of the low incoming wave height due to the sheltered location of the mussel patch with respect to the main wave direction. However interactions between currents, wind and waves influence the current direction and magnitude and therefore influence the flow routing effects. The main conclusions can then be summarized as:

- Interactions between currents, wind and waves play a major role at this study site, because wind stresses and waves enhance vertical mixing and influence the current directions near the mussel patch. Even small waves dominated the total bed shear stress, so these experienced conditions differ significantly from conditions in previous flume studies.
- Weak indications for flow routing around the mussel patch were obtained. However due to the low elevation of the mussel patch above its surroundings ($\sim 10cm$) together with an insufficient setup of measurement equipment, additional research is required to confirm flow routing effects around a mussel patch.
- TKE measurements that indicated increased vertical mixing due to a patch boundary demonstrated an advantage for the organization of mussels in a patch structure, since increased vertical mixing is generally linked to an increased food supply.

7 Recommendations

The height differences of the mussel patch with respect to its surroundings were relatively small, because the investigated mussel patch contained relatively young mussels. Studying an older mussel patch with a larger elevation difference might result in different hydrodynamic conditions as partial blockage of the flow due to the elevation of the mussel patch becomes more important. Another improvement might be a more isolated mussel patch, so that advection of turbulent kinetic energy from further located mussel or oyster patches could be canceled out. A more isolated mussel patch would also be convenient for obtaining possible flow routing effects as ADVs could be located close beside the mussel patch, so that the flow profile as a function of distance from the side of the mussel patch and the creation of shear-layer vortices as described by Zong and Nepf [2010] could be investigated for mussel patches in field conditions. Finally another location which is less sheltered for waves might be selected as relative wave height at the investigated location were relatively small.

More research is required with respect to the current oscillations that were obtained during specific wind conditions as it is unclear how and where these oscillations are created. Also measurement equipment could be deployed further downstream of the patch to study the duration of these oscillations. These oscillations might be beneficial for the food supply for mussels and oysters.

It would be useful to gain more information about the hydrodynamic parameters such as current velocities, TKE and Reynolds stress as a function of the height above the bed since other studies (e.g. Lassen et al. [2006]) showed that the maximum values of TKE and Reynolds stress are strongly dependent on the elevation above the bed. Also more details with respect to the height of the boundary layer could be obtained, so that the development of the boundary layer near the patch boundaries can be studied. Further studies in this area could place ADV sensors closer to the bed, because the bottom change is known to be negligible. An ideal solution for measuring the boundary layer height as a function of current velocity near a patch boundary would be the deployment of a flow profiler.

8 Acknowledgments

The Mosselwad project is funded by the Waddenfonds and the Dutch Ministry of Infrastructure and Environment. The measurement campaign could be performed due to the help of the technical staff of Utrecht University: Marcel van Maarseveen, Henk Markies, Chris Roosendaal and Bas van Dam and also assistance of Arno Kangeri from Imares was appreciated. Finally I would thank Maarten van der Vegt and Jasper Donker for their useful comments and discussions and Jasper Donker for arranging the field campaign.

References

- A.G. Brinkman, N. Dankers, and M. Van Stralen. An analysis of mussel bed habitats in the Dutch Wadden Sea. *Helgoland Marine Research*, 56:59–75, 2002.
- H. Charnock. Wind stress on a water surface. *Quarterly Journal of the Royal Meteorological Society*, 350:639–640, 1955.
- H.E. De Swart and J.T.F. Zimmerman. Morphodynamics of Tidal Inlet Systems. *Annual Review of Fluid Mechanics*, 41:203–229, 2009.
- C.G.N. De Vooy. Numbers of larvae and primary plantigrades of the mussel *Mytilus edulis* in the western Dutch Wadden Sea. *Journal of Sea Research*, 41:189–201, 1999.
- J.J.A. Donker, M. Van der Vegt, and P. Hoekstra. Wave forcing over an intertidal mussel bed. *Journal of Sea Research*, <http://dx.doi.org/10.1016/j.seares.2012.08.010>, 2012.
- G. Falkovich and K.R. Sreenivasan. Lessons from hydrodynamic turbulence. *Physics Today*, 59(4):43–49, 2006.
- F. Feddersen. Quality Controlling Surf Zone Acoustic Doppler Velocimeter Observations to Estimate the Turbulent Dissipation Rate. *Journal of Atmospheric and Oceanic Technology*, 27:2039–2055, 2010.
- F. Feddersen and A.J. Williams. Direct Estimation of the Reynolds Stress Vertical Structure in the Nearshore. *Journal of Atmospheric and Oceanic Technology*, 24: 102–116, 2007.
- F. Feddersen, J.H. Trowbridge, and A.J. Williams. Vertical structure of dissipation in the nearshore. *Journal of Physical Oceanography*, 37:1764–1777, 2007.
- A.M. Folkard and J.C. Gascoigne. Hydrodynamics of discontinuous mussel beds: Laboratory flume simulations. *Journal of Sea Research*, 62:250–257, 2009.
- M. Friedrichs and G. Graf. Characteristic flow patterns generated by macrozoobenthic structures. *Journal of Marine Systems*, 75:348–359, 2009.
- G.P. Gerbi, J.H. Trowbridge, E.A. Terray, A.J. Plueddemann, and T. Kukulka. Observations of Turbulence in the Ocean Surface Boundary Layer: Energetics and Transport. *Journal of Physical Oceanography*, 39:1077–1096, 2009.
- D.G. Goring and V.I. Nikora. Despiking Acoustic Doppler Velocimeter Data. *Journal of Hydraulic Engineering*, 117:117–126, 2002.
- W.D. Grant and O.S. Madsen. Combined wave and current interaction with a rough bottom. *Journal of Geophysical Research*, 84(C4):1797–1808, 1979.
- S.M. Henderson, R.T. Guza, S. Elgar, and T.H.C. Herbers. Refraction of Surface Gravity Waves by Shear Waves. *American Meteorology Society*, 36:629–635, 2006.
- T.H.C. Herbers, S. Elgar, and R.T. Guza. Directional spreading of waves in the nearshore. *Journal of Geophysical Research*, 104:7683–7693, 1999.

- G. Hilgerloh, M. Herlyn, and H. Michaelis. The influence of predation by herring gulls *Larus argentatus* and oystercatchers *Haematopus ostralegus* on a newly established mussel *Mytilus edulis* bed in autumn and winter. *Helgoland Meeresuntersuch*, 51:173–189, 1997.
- N.L. Jones and S.G. Monismith. The influence of whitecapping waves on the vertical structure of turbulence in a shallow estuarine embayment. *Journal of Physical Oceanography*, 38(7):1563–1580, 2008.
- J. Lassen, M. Kortegaard, H.U. Riisgard, M Friedrichs, G. Graf, and P.S. Larsen. Down-mixing of phytoplankton above filter-feeding mussels – interplay between water flow and biomixing. *Marine Ecology Progress Series*, 314:77–88, 2006.
- A. Lorke, B. Müller, A. Maerki, and A. Wüest. Breathing Sediments: The Control of Diffusive Transport across the Sediment: Water Interface by Periodic Boundary-Layer Turbulence. *Limnology and Oceanography*, 48:2077–2085, 2003.
- J.L. Lumley and E.A. Terray. Kinematics of turbulence convected by a random wave field. *Journal of Physical Oceanography*, 13(11):2000–2007, 1983.
- O.S. Madsen. Spectral wave-current boundary bottom boundary layer flows. *Coastal Engineering*, 94:384–397, 1994.
- S. McGroarty, J.D. Goss-Custard, and R.T. Clarke. Mussel *Mytilus edulis* (Mytilacea) dynamics in relation to environmental gradients and intraspecific interactions. *Netherlands Journal of Aquatic Ecology*, 27:163–171, 1993.
- Yelland M.J. and P.K. Taylor. Wind stress measurements from the open ocean. *Journal of Physical Oceanography*, 26:541–558, 1996.
- P. Nielsen. *Coastal Bottom Boundary Layers and Sediment Transport 4*. World Scientific, Singapore, SG, 1992.
- P.H. Nienhuis. Nutrient cycling and foodwebs in Dutch estuaries. *Hydrobiologia*, 265:15–44, 1993.
- A.R.M. Nowel and P.A. Jumars. Flow environments of aquatic benthos. *Annual Review of Ecology and Systematics*, 15:303–328, 1984.
- B. Okamura. Group living and the effects of spatial position in aggregations of *Mytilus edulis*. *Oecologia*, 69:341–347, 1986.
- A. Oost. *Dynamics and sedimentary development of the Dutch Wadden Sea, with emphasis on the Frisian inlet: A study of the barrier islands, ebb-tidal deltas, inlets, and drainage basins*. Faculty of Geosciences, University of Utrecht, Utrecht, The Netherlands, 1995.
- A. Pulfrich. Reproduction and recruitment in Schleswig Holstein Wadden Sea edible mussel (*Mytilus edulis*) populations. *Institut für Meereskunde, Christian-Albrechts Universität Kiel, Germany*, 1995.
- H.U. Riisgard, J. Lassen, M. Kortegaard, L.F. Møller, M Friedrichs, M.H. Jensen, and P.S. Larsen. Interplay between filter-feeding zoobenthos and hydrodynamics in the shallow Odense Fjord (Denmark) - earlier studies and recent studies,

- perspectives and modeling. *Estuarine, Coastal and Shelf Science*, 75:281–295, 2007.
- I.S. Robinson. Tidal vorticity and residual circulation. *Deep-Sea Research*, 28A(3): 195–212, 1981.
- S.D. Smith. Coefficients for a sea surface wind stress, heat flux and wind profiles as a function of wind speed and temperature. *Journal of Geophysical Research*, 93: 15467–15472, 1988.
- H. Tennekes and J.L. Lumley. *A First Course in Turbulence*. MIT press Design Department, 1972.
- E.A. Terray, M.A. Donelan, Y.C. Agrawal, W.M. Drennan, K.K. Kahma, A.J. Williams, P.A. Hwang, and S.A. Kitaigorodskii. Estimates of kinetic energy dissipation under breaking waves. *Journal of Physical Oceanography*, 26:792–807, 1996.
- J.H. Trowbridge. On a technique for measurement of turbulent shear stress in the presence of surface waves. *Journal of Atmospheric and Oceanic Technology*, 15: 290–298, 1998.
- J. Van de Koppel, M. Rietkerk, and P.M.J. Herman. Scale-dependent feedback and regular spatial patterns in young mussel beds. *The American Naturalist*, 165: E66–E77, 2005.
- L.A. Van Duren, P.M.J. Herman, A.J.J. Sandee, and C.H.R. Heip. Effects of mussel filtering activity on boundary layer structure. *Journal of Sea Research*, 55:3–14, 2006.
- B. Van Leeuwen, D.C.M. Augustijn, B.K. Van Wesenbeeck, S.J.M.H. Hulscher, and M.B. De Vries. Modeling the influence of a young mussel bed on fine sediment dynamics on an intertidal flat in the Wadden Sea. *Ecological Engineering*, 36: 145–153, 2010.
- L.C. Van Rijn. *Principles of fluid flow and surface waves in rivers, estuaries, seas and oceans*. Aqua Publications, Amsterdam, The Netherlands, 1990.
- W. Wang and R.X. Huang. Wind energy input to the surface waves. *Journal of Physical Oceanography*, 34:1276–1280, 2004.
- J. Widdows and M. Brinsley. Impact of biotic and abiotic processes on sediment dynamics and consequences to the structure and functioning of the intertidal zone. *Journal of Sea Research*, 48:143–156, 2002.
- J. Widdows, J.S. Lucas, M.D. Brinsley, P.N. Salkeld, and F.J. Staff. Investigation of the effects of current velocity on mussel feeding and mussel bed stability using an annular flume. *Helgoland Marine Research*, 56:3–12, 2002.
- L.D. Wright, L.C. Schaffner, and J.P.-Y. Maa. Biological mediation of bottom boundary layer processes and sediment suspension in the lower Chesapeake Bay. *Marine Geology*, 141:27–50, 1997.
- A. Wüest and A. Lorke. Small-Scale Hydrodynamics in Lakes. *Annual Review Fluid Mechanics*, 35:373–412, 2003.

L. Zong and H. Nepf. Flow and deposition in and around a finite patch of vegetation.
Geomorphology, 116:363–372, 2010.